



UNIVERSITY OF LEEDS

This is a repository copy of *Flow processes and sedimentation in contourite channels on the northwestern South China Sea margin: A joint 3D seismic and oceanographic perspective*.

White Rose Research Online URL for this paper:  
<http://eprints.whiterose.ac.uk/107683/>

Version: Accepted Version

---

**Article:**

Gong, C, Peakall, J, Wang, Y et al. (2 more authors) (2017) Flow processes and sedimentation in contourite channels on the northwestern South China Sea margin: A joint 3D seismic and oceanographic perspective. *Marine Geology*, 393. pp. 176-193. ISSN 0025-3227

<https://doi.org/10.1016/j.margeo.2016.11.002>

---

Published by Elsevier B.V. This manuscript version is made available under the CC-BY-NC-ND 4.0 license <https://creativecommons.org/licenses/by-nc-nd/4.0/>

**Reuse**

Unless indicated otherwise, fulltext items are protected by copyright with all rights reserved. The copyright exception in section 29 of the Copyright, Designs and Patents Act 1988 allows the making of a single copy solely for the purpose of non-commercial research or private study within the limits of fair dealing. The publisher or other rights-holder may allow further reproduction and re-use of this version - refer to the White Rose Research Online record for this item. Where records identify the publisher as the copyright holder, users can verify any specific terms of use on the publisher's website.

**Takedown**

If you consider content in White Rose Research Online to be in breach of UK law, please notify us by emailing [eprints@whiterose.ac.uk](mailto:eprints@whiterose.ac.uk) including the URL of the record and the reason for the withdrawal request.



[eprints@whiterose.ac.uk](mailto:eprints@whiterose.ac.uk)  
<https://eprints.whiterose.ac.uk/>

## Accepted Manuscript

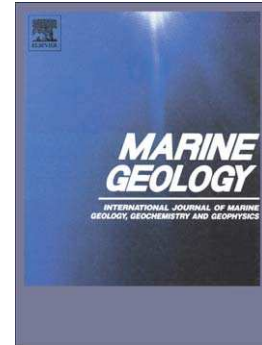
Flow processes and sedimentation in contourite channels on the northwestern South China Sea margin: A joint 3D seismic and oceanographic perspective

Chenglin Gong, Jeff Peakall, Yingmin Wang, Mathew G. Wells, Jie Xu

PII: S0025-3227(16)30297-3  
DOI: doi: [10.1016/j.margeo.2016.11.002](https://doi.org/10.1016/j.margeo.2016.11.002)  
Reference: MARGO 5538

To appear in: *Marine Geology*

Received date: 5 December 2015  
Revised date: 2 November 2016  
Accepted date: 10 November 2016



Please cite this article as: Gong, Chenglin, Peakall, Jeff, Wang, Yingmin, Wells, Mathew G., Xu, Jie, Flow processes and sedimentation in contourite channels on the northwestern South China Sea margin: A joint 3D seismic and oceanographic perspective, *Marine Geology* (2016), doi: [10.1016/j.margeo.2016.11.002](https://doi.org/10.1016/j.margeo.2016.11.002)

This is a PDF file of an unedited manuscript that has been accepted for publication. As a service to our customers we are providing this early version of the manuscript. The manuscript will undergo copyediting, typesetting, and review of the resulting proof before it is published in its final form. Please note that during the production process errors may be discovered which could affect the content, and all legal disclaimers that apply to the journal pertain.

# Flow processes and sedimentation in contourite channels on the northwestern South China Sea margin: A joint 3D seismic and oceanographic perspective

Chenglin Gong<sup>a\*</sup>, Jeff Peakall<sup>b</sup>, Yingmin Wang<sup>c</sup>, Mathew G. Wells<sup>d</sup>, Jie Xu<sup>a</sup>

<sup>a</sup>Bureau of Economic Geology, Jackson School of Geosciences, The University of Texas at Austin, Austin, Texas 78713, USA

<sup>b</sup>School of Earth and Environment, University of Leeds, Leeds, West Yorkshire LS2 9JT, UK

<sup>c</sup>Ocean College, Zhejiang University, Hangzhou, Zhejiang Province, 310058, People's Republic of China

<sup>d</sup>Department of Physical & Environmental Sciences, University of Toronto Scarborough, 1265 Military Trail, Toronto, ON M1C1A4, Canada

## ABSTRACT

3D seismic data from the northwestern South China Sea margin, coupled with the quantification of oceanographic processes and morphological results, were used to infer three-dimensional flow processes and in turn sedimentation in contourite channels. Contour currents resulting from the Northern Pacific Deep Water (NPDW-CCs) flowing through the bends of contourite channels around a topographic high lead to an imbalance in the transverse direction, around the bend, between three competing forces (i.e., upslope directed Coriolis forces versus downslope directed centrifugal and pressure-gradient forces). The interface deflection of NPDW-CCs by Coriolis, pressure gradient, and centrifugal forces yields a helical flow cell consisting of upper return flows directed downslope and basal flows orientated upslope. Ekman boundary layers, at the base and flow interface, are also likely present leading to flows in the downslope direction. The helical flow cell in the bulk of contour currents, and Ekman boundary layers, constitute a Coriolis force-induced helical flow circulation,

---

Correspondence: Bureau of Economic Geology, Jackson School of Geosciences, The University of Texas at Austin, PO Box X, Austin, TX 78713-8924, USA.  
E-mail: [chenglingong@hotmail.com](mailto:chenglingong@hotmail.com)

which we suggest promoted asymmetric intra-channel deposition (i.e., downslope deposition versus upslope erosion), forcing contourite channels to consistently migrate in an upslope direction. Such Coriolis force-induced helical flow circulation is evidenced by occurrence of volumetrically significant overbank deposits along downslope margins and by asymmetric channel cross-sections with steepened channel walls and truncation terminations along upslope margins. The Coriolis force-induced helical flow circulation exhibits subcritical flow conditions (represented by internal Froude numbers estimated as 0.04 to 0.19), and is sufficiently deep to spill out of the studied contourite channels, yielding overbank deposits along the downslope flanks of the contourite channels.

**Keywords:** Contourite channels, northwestern South China Sea margin, Coriolis forces, helical flow circulation, Ekman boundary layer

## 1. Introduction

On the basis of sediment transport processes, two different types of deep-water channels have been recognized and extensively documented in the literature, namely turbidite channels created predominantly by downslope sediment density flows (e.g., Menard, 1955; Wynn et al., 2007; Pyles et al., 2012; Kane et al., 2013) and contourite channels produced by alongslope contour currents (e.g., Heezen and Hollister, 1964; Faugères et al., 1993, 1999; Hernández-Molina et al., 2014). Both turbidite and contourite channels have been the subject of increasingly intense studies in recent years (e.g., Viana and Faugères, 1998; Wynn et al., 2007; Pyles et al., 2012; Kane et al., 2013; Rebesco et al., 2014; Sylvester and Covault, 2016). This is largely because they: (1) are long-lived features that are common on Earth's siliciclastic continental margins (e.g., Normark, 1970; Wynn et al., 2007; Peakall et al., 2012; Kane et al., 2013; Hernández-Molina et al., 2014); (2) serve as effective conduits for the delivery of sediment and organic material into deep-water settings (e.g., Menard, 1955; Shepard and Emery, 1973; Clift and Gaedicke, 2002; Galy et al., 2007; Peakall and Sumner, 2015); and (3) are repositories for substantial amounts of coarse-grained sediments on and beyond the continental slope. In the case of turbidites these deposits have proven to be one of the most common types of deep-water reservoirs, whilst sandy contourites have great potential to act as reservoirs (e.g., McHargue et al., 2011; Stow et al., 2013; Gong et al., 2016).

In recent years, an increasing effort has been made to understand flow dynamics of turbidite channels through sedimentological analysis of outcrops (e.g., Dykstra and

Kneller, 2009; Pyles et al., 2012), direct measurement of density flows in modern sinuous submarine channels and similar downslope analogs (e.g., Vangriesheim et al., 2009; Parsons et al., 2010; Sumner et al., 2014), physical experiments (e.g., Corney et al., 2006; Keevil et al., 2006; Peakall et al., 2007; Cossu and Wells, 2010, 2013; Ezz et al., 2013; Janocko et al., 2013; Cossu et al., 2015), and numerical simulations (e.g., Corney et al., 2006; Imran et al., 2007; Giorgio Serchi et al., 2011; Dorrell et al., 2013; Janocko et al., 2013; Ezz and Imran, 2014). However, whilst there is a good understanding of the underlying flow processes in contourite channels (e.g., Faugères et al., 1993; Rebesco, 2005; Faugères and Stow, 2008; Rebesco et al., 2014), the detailed three-dimensional flow dynamics and their control on sedimentation in isobath-parallel contourite channels remain comparatively poorly studied. The occurrence of previously undocumented, seismically well-imaged contourite channels on the northwestern South China Sea margin, together with an extensive (ca 3000 km<sup>2</sup>), high-quality (ca 10 m vertical and 12.5 m lateral resolution), time-migrated 3D seismic database (Figs. 1 and 2), make the study area a suitable place to study how the interplay of Coriolis, centrifugal, and pressure forces control sedimentation in contourite channels. Using integrated 3D seismic data and the quantification of oceanographic processes, the current work addresses three-dimensional flow dynamics and sedimentation patterns of a contourite channel on the northwestern South China Sea margin. Results from this study contribute to an improved understanding of the role of contour currents and Coriolis, pressure gradient, and centrifugal forces in shaping sedimentation in deep-water channels.

## 2. Geological and oceanographic background

### 2.1. Geological context

Our study area is located on the northwestern South China Sea margin (Figs. 1A and 1B), which was created by the convergence between the Eurasian and Philippine Sea plates (e.g., Peron-Pinvidic et al., 2013). The northwestern South China Sea margin experienced three stages of tectonic-stratigraphic evolution, namely a rifting stage from 45 to 21 Ma, a rift-drift transition stage from 21 to 10.5 Ma, and a drifting stage from 10.5 Ma to present (e.g., Gong et al., 2014; Zhao et al., 2015a). Accordingly, the basin infill of the northwestern South China Sea margin can be divided into three supersequences, namely an Eocene to Oligocene synrift supersequence, an early to middle Miocene rift-drift supersequence, and a late Miocene to Quaternary drifting supersequence (e.g., Gong et al., 2014). Depositional systems formed in neritic, deltaic and nearshore environments became prevalent within the synrift and rift-drift supersequences, whereas 'typical' deep-water systems and coeval shallow-water systems were well developed within the drifting supersequence, in response to the development of a prominent shelf-slope-basin physiography (e.g., Gong et al., 2014; Zhao et al., 2015a). Deep-water channels, as evident on bathymetric maps of the modern seafloor of the study area, were developed within the drifting supersequence of the northwestern South China Sea margin, and are the focus of this study (Figs. 1B and 2). In particular, the current study focuses on curved channels around a pre-existing topographic high seen in bathymetric maps of Fig. 2.

## 2.2. Oceanographic context

Modern oceanic circulation in the South China Sea shows a “sandwich” pattern consisting of seasonal surface-water circulation ( $<26 \text{ kg/m}^3\sigma_0$ ), intermediate water circulation resulting from the North Pacific Intermediate Water (NPIW) (26 to  $27.3 \text{ kg/m}^3\sigma_0$ ), and deep-water circulation resulting from the Northern Pacific Deep Water (NPDW) ( $>27.3 \text{ kg/m}^3\sigma_0$ ) (Yang et al., 2010; Gong et al., 2015; He et al., 2013) (Fig. 1A). The seasonal surface-water circulation with effective depth of  $<350 \text{ m}$  is driven by monsoons, and is clockwise in the summer, but counter-clockwise during the winter (Zhu et al., 2010; He et al., 2013). It has temperature ranges of  $17$  to  $20^\circ\text{C}$  and salinity ranges of  $34.60$  to  $34.65$  (Yang et al., 2010). Intermediate water circulation is clockwise with an effective depth of  $350$  to  $1350 \text{ m}$ , and is characterized by temperature ranges of  $7$  to  $10^\circ\text{C}$  and salinity ranges of  $34.35$  to  $34.43$  (Yang et al., 2010; Gong et al., 2015) (Fig.1). Deep-water circulation is counter-clockwise with an effective depth of  $>1350 \text{ m}$ , and has temperature ranges of  $2$  to  $7^\circ\text{C}$  and salinity ranges of ca  $34.60$  to  $34.58$  (Yang et al., 2010; Gong et al., 2015) (Fig.1). Contour-flowing currents of NPDW–CCs are interpreted to play a pivotal role in controlling deep-water sedimentation on the continental slope and the adjacent abyssal plain, resulting in contourite drifts near the ODP site 1144 and fine-grained bottom-current sediment waves on the abyssal plain (e.g., Li et al., 2013; Gong et al., 2015). The effects of NPDW–CCs in controlling sedimentation in contourite channels are the focus of the present study.

## 3. Database and methodology

### 3.1. Seismic data interpretation

The primary source of the datasets used in this study is ca3000 km<sup>2</sup> of 3D seismic data, acquired from the northwestern South China Sea margin (Figs. 1 and 2). The frequency of the time-migrated volume varies with depth, but is approximately 30 Hz for the study interval of interest, yielding an estimated vertical resolution of ca 12.5 m. 3D seismic reflection data have a 4-ms vertical sampling rate and bin spacing of 25 × 12.5 m. They were processed to zero phase and were displayed using ‘SEG reverse polarity’, where an increase in acoustic impedance is represented by a positive (peak) reflection event.

This work integrates “classical” 2D seismic facies analysis with the 3D seismic geomorphology approach, through which seismic stratigraphy and geomorphology of the interpreted channels are quantitatively analyzed. Root-mean-square (RMS) amplitude that calculates the square root of the sum of the time-domain energy, together with seismic amplitude cubes, offer enhanced visualization of the stratigraphic architecture of small-scale depositional elements. They are, thus, used to delineate architectural styles of the interpreted channels and concomitant depositional elements, and were created via the following two steps. The first step was to flatten the 3D seismic amplitude volumes using the seafloor as the hanging horizon (0 ms). The second step was to create 3D seismic amplitude cubes and 3D RMS attribute probes.

### 3.2. Quantitative analysis

Several numerical approaches were employed to quantitatively document

morphometric properties and stacking patterns of the documented channels. They are: channel aspect ratios ( $W/T$ , dimensionless) and channel migration to aggradation ratios ( $L_m/V_a$ , dimensionless), which are, respectively, given by:

$$\text{Channel aspect ratios} = W/T \quad (1)$$

$$\text{Channel migration to aggradation ratios} = dx/dy \quad (2)$$

Where  $W$  is the average channel width,  $T$  is the average channel thickness,  $dx$  ( $L_m$ ) is the lateral component (lateral migration component) of a specific channel-growth trajectory, and  $dy$  ( $V_a$ ) is the vertical component (vertical aggradation component) of a given channel-growth pathway. Direct measurements of  $W$ ,  $T$ ,  $dx$ , and  $dy$  were converted from time to depth, using an average velocity of 2003 m/s for the shallow siliciclastics and 1500 m/s for seawater, as calculated from well YC 35-1-2 (see Fig. 1 for well location). The component of channel-growth trajectories (reported as  $L_m/V_a$ ) is an additional means, through which stacking patterns of the documented channels can be quantitatively documented and differentiated.

#### 4. Seismic geomorphology and stratigraphy

Examination of 2D seismic lines and 3D time slices allowed the differentiation of three main seismic facies (Figs. 3 to 6). See Table 1 for a complete description and interpretation of them.

##### 4.1. Seismic facies description

###### 4.1.1. Alongslope seismic facies

In cross-sectional view, alongslope seismic facies are seen as lens-shaped, continuous low- to mid-amplitude reflections (Figs. 5 and 6, and Table 1). Their bases

are marked by V- or U-shaped basal bounding surfaces, truncation of underlying units, and with surfaces onlapping onto these bounding surfaces (Figs. 5 and 6, and Table 1). Morphologically, alongslope seismic facies are approximately 3–5 km wide (W) (averaging 4.1 km) and 175–253m deep (T) (averaging 225 m), giving rise to relatively low W/T of 12–25 (averaging 18) (Fig. 7B, and Table 2), as compared to downslope seismic facies discussed below. One of the most distinctive morphological characteristics of them is that their upslope walls are, overall, steeper than their downslope counterparts, resulting in asymmetrical cross-sectional geometries (Figs. 5 and 6).

In plan view, alongslope seismic facies are expressed on seismic amplitude slices as low amplitude bands (Figs. 3, 4, and 8A to 10A), and manifest on 3D RMS attribute volumes as low RMS-attribute bands (Figs. 8B to 10B, and Table 1). They show slightly sinuous channel courses of ca 10s kilometres long, and are orientated parallel or subparallel to the regional contour lines (Figs. 1B, 2, 3 to 4, and 8 to 10).

#### 4.1.2. Overbank seismic facies

In cross-sectional profile, reflectors in the central part of the overbank seismic facies are generally well-layered, low amplitude, and laterally continuous (Figs. 5 and 6, and Table 1). They are bounded at their base by a prominent high-amplitude reflection, which separates the overlying well-layered, parallel to subparallel, continuous seismic reflections from the underlying strata that are intensively cut by polygonal faults (Fig. 6A). Reflectors on the upslope margins of the overbank seismic facies (i.e., margins against the alongslope seismic facies) are commonly associated

with discontinuous and even truncated reflections (Figs. 5A, 5B, and 6A). Their thicknesses (T) varies from 0 m to 200 m, with a mean value of  $T=150$  m (Figs. 5 and 6).

In planform, overbank seismic facies occur along the left-hand sides of the alongslope seismic facies (looking from east to west) (Fig. 5 to 6 and 8 to 10). They extend in both dip and strike views for 10s km, extend in the strike view for tens of kilometres, and occupy an area of up to 100s km<sup>2</sup> (Fig. 5 to 6 and 8 to 10). They are expressed on the flattened horizontal seismic amplitude slices as fan-shaped low seismic amplitude sheets, and appear on the flattened horizontal RMS-attribute slices as fan-shaped low RMS-attribute accumulations (Figs. 8 to 10).

#### 4.1.3. Downslope seismic facies

Downslope seismic facies are made up of continuous to discontinuous, moderate- to high-amplitude reflections (Fig. 11). They appear on time slices as wide, north-south-trending high- or low-amplitude bands (Figs. 8A to 10A). They are seen in RMS attribute-extraction maps as wide, high- or low-RMS attribute sheets (Figs. 8B to 10B). One of the most distinctive architectural properties of the downslope seismic facies is that they consistently migrated to the SW for a few kilometres, resulting in wide lateral channel migration (Fig. 11).

Downslope seismic facies are made up of two discrete channel-complex sets (CCS1 and CCS2) that are seismically resolvable (Fig. 11). CCS1 and CCS2 are, overall, short and relatively straight, and are a few tens of kilometres in length and 0 – 95 m in thickness (Fig. 12). They are characterized by W of 7.7 to 11.2 km (averaging

9.0 km), T of 79 to 155 m (averaging 115 m), and W/T of 63 to 109 (averaging 81) (Fig. 7, and Table 3).

## 4.2. Sedimentologic interpretation

### 4.2.1. Alongslope seismic facies: Contourite channels

Alongslope seismic facies are orientated parallel or subparallel to regional isobaths (Figs. 5 to 6 and 8 to 10, and Table 1). The channels are characterized by small channel aspect ratios (~3-5; Fig. 7), exhibit little lateral channel migration ( $L_m$  of 0.6 to 2.1 km, with a mean value of  $L_m = 1.4$  km) relative to vertical channel aggradation ( $V_a$  of 49 – 221 m, with a mean value of  $V_a = 146$  m) (red triangles in Fig.13A), and display clear upslope migration (reported as low  $L_m/V_a$  of ca 5 to 10) (Figs. 5A, 6A, and 14A, and Table 2). These channel geometries are in marked contrast to the downslope channels observed, which are much wider and shallower (Fig. 7), and exhibit lateral migration that is an order of magnitude greater than that observed for the alongslope channels (Fig. 13). Furthermore, the basal surface of the present alongslope channel is characterised by marked topography, and in places the channel shallows downstream. Such topography is atypical of turbidite channels where suspension driven deposition would normally ‘heal’ such topography, leading to slopes that gradually decrease downslope (Kneller, 2003). Finally, deposits on the upslope side are deposited at greater elevations than those on the downslope overbank side, reflecting that flow super-elevation was towards the inner bend, rather than the outer bend as is typically observed in turbidite channels (Peakall and Sumner, 2015). In contrast, all these observations are commonly related to alongslope contour

currents (i.e., contourite currents) (e.g., Brackenridge et al., 2013; Stow et al., 2013; Hernández-Molina et al., 2014; Gong et al., 2015).

In addition, the documented alongslope channels are separated from the coeval shelf and upper slope by the isobath-subparallel Xisha Trough (Fig. 1A). The Xisha Trough is U-shaped in cross-sectional view, and has relief of ca. 100 to 500 m and width of 6.4 to 13.8 km (Liu and Wu, 2006), yielding a significant negative topographic relief. This pronounced negative topographic relief would have acted as the physiographic “container” and accommodation space for many turbidity currents, resulting in a giant, S-shaped, slope-subparallel submarine canyon, with length of ca 425 km, width of ca 3 to 12 km, and area of ca 50,000 km<sup>2</sup> (see Gong et al., 2011 for a detailed discussion) (i.e., central submarine canyon in Fig. 1A). Turbidity currents derived from the upper slope or contemporaneous feeder systems (i.e., rivers draining southeastern Hainan Island or eastern Vietnam) would, thus, preferentially be captured by this physiographic “container”. This, together with the fact that the documented alongslope channels are approximately 15 km far away from the coeval downslope channels as discussed later (Figs. 8 to 10), further suggest that the alongslope channels are the product of contourites. Turbidity currents do not therefore appear to play a significant role in the modulation of flow processes in the slope parallel channels. Herein, we focus on the flow processes and sedimentation in these contourite channels.

#### 4.2.2. Overbank seismic facies: Overbank deposits

Overbank seismic facies were developed at the sharp bends of the interpreted

channels (Fig. 2, 8 to 10, and 15), and this areal distribution of overbank seismic facies suggests that these are not classical mounded drifts (e.g., Faugères and Stow, 2008; Hernández-Molina et al., 2014). The facies occurs in overbank settings of the interpreted channels, and appear to be created by overbank flows at the sharp bends, as discussed in Section 6.2, giving rise to overbank deposits (Figs. 5, 6, and 14, and Table 1).

In addition, levee crests are seen to develop immediately below the basal bounding surface of the interpreted overbank deposits (Figs. 6A, 6C, and 14A). They show an overall mounded and downlapping character in cross-sectional view (see downlap terminations marked as red dots in Fig. 6C). They appear in plan-view time slices as alternating sets of closely spaced, crescent-shaped, high- and low amplitude threads (Figs. 4A and 4B). They are regionally localized, and occur at the sharp bends of the slope parallel channels (Figs. 2, 4A and 4B). Similar mounded, stacked, downlapping seismic reflection packages have also been observed on the Amazon and Hueneme fans (Piper and Normark, 2001) and in the Einstein channel-levee system (Ezz et al., 2014), and were interpreted to be created by flow stripping (e.g., Piper and Normark, 1983). These levee crests appear to diminish in an upsection direction, disappearing at the basal bounding surface of the overbank seismic facies, and were then draped by well-layered, parallel to subparallel, continuous reflections (Figs. 3 and 6C). Downlap terminations as seen in the older levee crests are absent in the upper overbank seismic facies, strongly suggesting the progressive draping of levee crests by overbank flows as discussed in Section 6.2 (Figs. 3 and 6C).

Given the presence of both alongslope and downslope channels in the dataset, reflecting a mixed turbidite-contourite system in this geographic area, then a key question is whether turbidity currents played a role in the slope parallel channels, and if this is reflected in their overbank deposits. Turbidite levees and contourite mounds exhibit many similarities including low amplitude, continuous reflectors in seismic, and the presence of levee-crest geometries (e.g., Piper and Normark, 2001; Rebesco et al., 2014). Whilst, the presence of a turbiditic component, particularly in the lowermost deposits characterized at the bend apex by levee-crest geometries, cannot be easily ruled out, the observed geometric differences between the alongslope and downslope channels strongly suggest that these channels are dominantly contourite driven. In particular, the alongslope channels are much narrower, migrate upslope, and show deposits on the upslope side that are higher than those on the downslope side (see Section 4.2.1 for further details).

#### 4.2.3. Downslope seismic facies: Unidirectionally migrating deep-water channels

Downslope seismic facies, which are orientated roughly perpendicular to isobaths and developed on continental slopes, are commonly interpreted to be deep-water channels (e.g., Wynn et al., 2007; Gong et al., 2013; Janocko et al., 2013). They differentiate from other well-documented turbidite channels by long-term (Million-year scale), persistently unidirectional channel trajectories (Fig. 11A), forming unidirectionally migrating deep-water channels (see Gong et al., 2013, 2016 for a detailed interpretation). They exhibit wide lateral channel migration (measured as high  $L_m$  of 9.2 to 21.3 km, with a mean value of  $L_m = 17.5$  km) relative to vertical

channel aggradation (measured as low  $V_a$  of 185 to 251 m, with a mean value of  $V_a = 227$  m) (blue dots in Fig. 13A), giving rise to wide lateral channel migration (represented by high  $L_m/V_a$  of ca 72 to 90, with a mean value of  $L_m/V_a = 78$ ) (blue dots in Fig.13B).

In addition, unidirectionally migrating deep-water channels are isolated and are far away from the coeval contourite channels (Figs. 8 to 10). They are not linked to coeval shelf edges, and initiated at the middle to lower slope of the southwestern South China Sea margin, with their heads located at some point beyond the northern border of the 3D seismic volume used in this work (Figs. 8 to 10 and 11B). These two lines of argument, coupled with the fact that they are separated from the contemporaneous shelf edge by the depositional strike-orientated Xisha Trough (Fig. 1A), suggest that the downslope seismic facies were probably triggered by small-scale instability or localized collapses of the middle to lower northwestern South China Sea slope.

## 5. Flow dynamics of the documented contourite channels

### 5.1. Alongslope contour currents of NPDW-CCs with effective depth of >1350 m

Previous studies suggest that NPDW from the Pacific Ocean exchanged freely with the South China Sea since at least the Early Miocene (Zhu et al., 2010; Gong et al., 2013) (Fig. 1A). Geostrophic contour currents usually involve significant water mass over large areas and persist for very long time intervals of up to millions of years (e.g., Shanmugam, 2008; Stow et al., 2008; Gong et al., 2015). This, in turn, suggests that NPDW-CCs with effective depth of >1350 m were probably involved in

the construction of the interpreted channels distributed in water depths of  $>1300$  m, forming contourite channels and concomitant unidirectionally migrating deep-water channels (Figs. 8 to 11). Gong et al. (2013, 2016) have also attributed the long term unidirectional migration of deep-water turbidite channels, as recorded by downslope seismic facies, to the interaction of downslope gravity currents with contour currents that have predominantly unidirectional flow conditions.

Preliminary bedform-velocity analysis by Gong et al. (2015), coupled with field measurements by Yang et al. (2010) and Zhao et al. (2015b), suggests that NPDW-CCs have a maximum flow velocity of ca 3 to 7 cm/s. Such slow contour current flow speeds are likely amplified as water is deflected around the topographic high or as they flow through the narrow conduit around the topographic obstruction (Fig. 2; Brackenridge et al., 2013). For example, contour currents resulting from Mediterranean Outflow Water are thought to locally reach velocities in excess of 2.5 m/s when they flow through the narrow gateway of the Strait of Gibraltar (Mulder et al., 2003). We, therefore, assume that NPDW-CCs have maximum velocities of 3 to 10 cm/s, when they flow through narrow contourite channels around a topographic high (Figs. 2 and 15A).

## 5.2. Coriolis forces directed towards the upslope margins

Coriolis forces have been experimentally proven to influence helical flow structures in many submarine turbidite channels, in marked contrast to rivers where Coriolis forces are negligible (Cossu and Wells, 2010, 2013). The relative influence of Coriolis forces on secondary flow fields in deep-water channels is measured via the

Rossby number ( $R_0$ ), which is defined by:

$$R_0 = |U/Wf| \quad (3) \quad (\text{Cossu and Wells, 2013})$$

where  $U$  is the mean velocity (ca 3 to 10 cm/s for NPDW-CCs),  $W$  is the average channel width (ca 4.1 km for the interpreted channels) (Table 2), and  $f$  is the Coriolis parameter defined as  $f = 2\Omega \sin(\theta)$ , with  $\Omega$  being the Earth's rotation rate and  $\theta$  being the latitude (ca 15.5° north for the studied channels).

Therefore, when  $U = 0.03 \text{ m sec}^{-1}$ ,  $R_0 = |0.03/(4100 \times 2\Omega \sin 15.5^\circ)| \approx 0.44$ ; or when  $U = 0.10 \text{ m sec}^{-1}$ ,  $R_0 = |0.10/(4500 \times 2\Omega \sin 15.5^\circ)| \approx 0.62$ . In both cases,  $R_0$  is  $\ll 1$ , suggesting that, no matter how strong (up to  $0.10 \text{ m sec}^{-1}$ ) or weak (down to  $0.03 \text{ m sec}^{-1}$ ) contour currents of NPDW-CCs may be, Coriolis forces (Figs. 14B, 14C, and 15B) always play a pivotal role in the modulation of the secondary flow structures in the studied channels (Thomson et al., 2010; Cossu and Wells, 2013). In the Northern Hemisphere, Coriolis forces will deflect the bulk flow to the right hand side, as looking downstream (e.g., Cossu and Wells, 2010, 2013; Cossu et al., 2015). This, in turn, leads to the superelevation of the flow on the right-hand side, up against the upslope side (e.g., Cossu and Wells, 2013). Associated with this, the downstream velocity core (the fastest part of the flow) is also focused against this outer (i.e., upslope) bank (e.g., Cossu and Wells, 2010, 2013; Cossu et al., 2015) (Figs. 14B, 14C, and 15B).

### 5.3. Coriolis-driven Ekman boundary layers directed towards the downslope margins

Ekman boundary layers should also be created by Coriolis forces as shown numerically for straight submarine channels at the lower and upper interfaces of the

flow (Wählin, 2004; Cossu et al., 2010), and in field data from straight contourite currents (Johnson and Sandford, 1992). The basal Ekman boundary layer has been shown to play a critical role in determining the sedimentary flow structures (Cossu and Wells, 2010, 2013). Ekman boundary layers will be directed to the left (looking downstream, from east to west), suggesting that the Coriolis-driven Ekman boundary layers would deflect the basal flow of NPDW-CCs to the downslope margins of the studied channels (Cossu and Wells., 2010; Cossu et al., 2010; Thomson et al., 2010) (Figs. 14B, 14 C, and 15B). Such Coriolis-driven Ekman boundary layers should theoretically be present below the main secondary circulation driven by the Coriolis forces (Cossu and Wells, 2010; Cossu et al., 2010), as described in Section 5.2.

#### 5.4. Centrifugal forces directed towards the downslope margins

A topographic high occurs along the right-hand sides of the interpreted channels (looking from east to west), and predated their formation (Figs. 2 and 15A). It might act to sculpt and shape the main contour current cores of NPDW-CCs travelling around a bend with a well-defined radius (Figs. 2 and 15A), suggesting that centrifugal forces created by the tangential velocity (Figs.14B, 14C, and 15B) probably influenced secondary flow fields in the studied channels. Centrifugal forces act away from the centre of curvature, and are therefore directed downslope (Figs. 14B, 14 C, and 15B). They show a vertical structure as governed by the vertical velocity profile (Corney et al., 2006, 2008; Dorrell et al., 2013; Peakall and Sumner, 2015), with low density stratification induced by the likely presence of fine-grained sediment, leading to the vertical position of the downstream velocity ( $U_{\max}$ ) being

located high in the flow (Corney et al., 2008; Peakall and Sumner, 2015). In turn this will result in the strongest centrifugally-driven flow in the upper parts of the current, acting towards the downslope side, partly offsetting the growth of Coriolis induced superelevation (Figs.14 and 15).

#### 5.5. Pressure-gradient forces directed towards the downslope margins

Recent studies investigating flow properties at submarine channel bends have focused on helical flow structures induced by the centrifugal force which sets up a superelevation of the flow (e.g., Corney et al., 2006; Parsons et al., 2010; Janocko et al., 2013). In turn, this superelevation sets up an opposing pressure-gradient force that acts away from the superelevation (e.g., Corney et al., 2006; Keevil et al., 2006; Imran et al., 2007; Dorrell et al., 2013; Janocko et al., 2013; Sumner et al., 2014). As Coriolis forces are estimated to be dominant in the documented contourite channels, superelevation is highest on the upslope margin, as shown by the deposits of draped material there at greater topographic heights than the main sediment-drift (see Figs. 2 and 15A). Consequently, the pressure-gradient force acts towards the downslope margin of the studied channels (white arrows on Figs. 14 and 15).

### 6. Sedimentation styles in contourite channels

#### 6.1. Helical flow circulation created by the transverse tilt of contour currents

In summary, four competing forces are generated when contour currents of NPDW-CCs flow through the interpreted channels. Coriolis forces direct the bulk flow upslope and set up flow superelevation on the upslope side (Figs. 14B, 14C, and 15B). Models also predict that there will be thin downslope orientated Coriolis-driven

Ekman boundary at the base, and upper interface, of the flow (Wåhlin, 2004; Cossu et al., 2010) (Figs. 14B, 14C, and 15B). Opposing the Coriolis force that acts on the bulk flow are the centrifugal forces and the pressure-gradient forces (red and white arrows in Figs. 14B and 15B, respectively). Centrifugal forces have a pronounced vertical structure and increase upwards away from the bed, whereas pressure-gradient forces are constant through the depth of NDPW-CCs (e.g., Corney et al., 2006, 2008). The interplay of upslope directed Coriolis forces versus downslope directed pressure-gradient and centrifugal forces acting on the NDPW-CCs, therefore, yields an imbalance, through the flow depth, and resultant transverse tilt of contour currents within the studied channels (e.g., Cossu et al., 2010, 2013). This, in turn, sets up a primarily Coriolis force-induced helical flow circulation composed of a large-scale secondary cell and Ekman boundary layers at the lower and upper interfaces (Figs. 14B, 14C, and 15B). The base of the main secondary flow cell is directed upslope as Coriolis forces exceed radial pressure gradient and centrifugal forces, whereas the top of the flow is directed towards the downslope side of the interpreted channels as pressure gradient and centrifugal forces dominate near the free surface. A thin downslope orientated Coriolis-driven Ekman boundary layer will be present at the very base of the along-channel flows (Figs. 14B, 14C, and 15B).

## 6.2. Superelevation and overspill

Recent studies in turbidite channels show that superelevation and overspill (if present) are very important in determining the orientation of the secondary flows (Dorrell et al., 2013; Sumner et al., 2014; Peakall and Sumner, 2015). However, in

turbidite channels, superelevation and overspill commonly occur at outer banks (Dorrell et al., 2013; Peakall and Sumner, 2015). In the interpreted contourite channels, superelevation is present on the upslope side, and overspill must clearly occur on the downslope side in order to build volumetrically extensive overbank deposits (Figs. 14B, 14C, and 15B). Therefore, the overbank flow may act to partly offset the growth of the superelevated flow on the upslope side, but the draped sedimentation on the upslope side demonstrates that overspill is not the dominant process that it can be in sinuous turbidite channels (Dorrell et al., 2013). The sedimentation patterns do show however that cross-stream flows in the studied channels are characterized by flow heights ( $h$ ) that exceed channel depths (reported as  $h \geq 150\text{--}250$  m for the interpreted contourite channels). Flow heights in excess of channel depths are common for turbidite channels (Peakall et al., 2000; Mohrig and Buttle, 2007; Pyles et al., 2012).

### 6.3. Parameterizing Coriolis force-induced helical flow rotation across topographic highs

There is a prominent topographic obstruction (i.e., sill seen in the bathymetric map half way around the illustrated channel in Figs. 2 and 15A) across the path of the along-channel flows. Such topographic obstacles have been suggested to induce oscillations on secondary flows (Thomson et al., 2010). The internal Froude number ( $F_r$ ) is employed to examine the effect of topographic highs on the interface between contour currents and the overlying water column, and is defined as:

$$F_r = \frac{U}{\sqrt{g'h}} \quad (4) \text{ (Kneller and Buckee, 2000)}$$

where  $g'$  is the reduced gravity of the interface between the contour currents and the overlying water column, and equals to  $g \times (\Delta\rho/\rho_0)$ , so that:

$$F_r = \frac{U}{\sqrt{g'h}} = \frac{U}{\sqrt{[g \times (\Delta\rho/\rho_0) \times h]}} \quad (5)$$

where  $U$  is the mean downstream velocity,  $g$  is the vertical acceleration due to gravity ( $9.8 \text{ m/s}^2$ ),  $\Delta\rho$  is the bulk density difference between the contour currents and the overlying water mass,  $\rho_0$  is the density of sea water (ca  $1027 \text{ kg/m}^3$ ), and  $h$  is the thickness of cross-stream flows in the studied channels (ca 150 to 250 m for the studied channels). Yang et al. (2010) suggest that Northern Pacific Deep Water involved in the construction of the studied channels has a persistent density difference ( $\Delta\rho$ ) of ca  $0.2 \text{ kg/m}^3$ .

Therefore, using equation 5, when  $U = 0.03 \text{ m sec}^{-1}$ ,  $F_r$  are calculated to range from 0.04 to 0.06; or when  $U = 0.1 \text{ m sec}^{-1}$ ,  $F_r$  are reconstructed to vary from 0.14 to 0.19. In both cases,  $F_r$  are  $< 1$  (reported as  $F_r = 0.04$  to  $0.19$ ), suggesting that secondary flows in the documented contourite channels display subcritical flow regimes (Kneller and Buckee, 2000, and references therein). This suggests that overflowing currents are subcritical, and as a result of deceleration will rapidly become depositional, giving rise to the overbank deposits along the downslope margins of the studied channels (Figs. 14 and 15).

#### 6.4. Sedimentation in contourite channels

Contour currents may carry in suspension muddy fines and particulate organic matter, forming significant nepheloid layers with the average thicknesses of ca 150 to 1500 m and average concentrations of suspended matter of 0.01 to 0.5 mg/L (McCave,

2008; Rebesco et al., 2014). The aforementioned Coriolis-force induced helical flow rotation consists of an upper return flow towards the downslope and a lower basal flow towards the upslope with a thin downslope orientated Coriolis-driven Ekman boundary layer at the very base. There will also be corresponding changes in the position of the downstream velocity core, which is positioned against the topographic high (Figs. 14 and 15). Such secondary flow structures are shown by the following two lines of evidence. Firstly, more intense erosion preferentially occurs along the upslope margins of the interpreted channels, as evidenced by asymmetric channel cross sections with steeper channel walls and widespread occurrence of truncation terminations along the upslope margins (Figs. 2, 5A, 6A, 14A, and 15A). Secondly, deposition preferentially happens along the downslope margins of the documented channels, as suggested by gentler channel walls and volumetrically extensive overbank deposits near the downslope sides (Figs. 2, 5A, 6A, 14A, and 15A). These observations suggest that Coriolis force-induced helical flow rotation in the studied channels favoured upslope-margin erosion induced by the high-velocity core near the upslope margin, but promoted downslope-margin deposition created by the overbank flow from the upper parts of the flow along the downslope flank (Figs. 14 and 15). Additionally, the combination of the basal Ekman boundary layer, the centrifugal force, and pressure-gradient induced force will act to move material in suspension immediately above the bed, and bedload towards the downslope side, accreting material to the inner part of the overbank deposits (Figs. 14 and 15). In combination, the interpreted Coriolis force-induced helical flow circulation results in asymmetric

deposition-and-erosion patterns and the resultant upslope migration of the interpreted channels (Figs.14 and 15).

## 7. Conceptual implications

The present model for the NPDW-CCs provides insight into three-dimensional flow fields in contourite currents and their linkage to sedimentation. This study and its comparison with experimental, analytical and numerical work on turbidite channels at low and high latitudes suggests that three-dimensional flow fields in a contourite channel on the northwestern South China Sea margin are more complicated than a single helical flow cell (cf. Hernandez-Molina et al., 2008; Rebesco et al., 2014), and that it combines a helical flow cell in the bulk of the flow and lower and upper Ekman boundary layers which are enhanced by the pressure-gradient force caused by flow superelevation. Where contourite channels exhibit curvature induced by pre-existing topography then these Ekman layers can also be enhanced (or reduced) by centrifugal forces depending on the orientation of the curvature. Specific to the present South China Sea case, the Ekman boundary layers are enhanced by centrifugal forces (Figs. 14B, 14C, and 15B). In the opposite case where the centrifugal force opposes the Ekman layers, then at a given, but as yet unknown, Rossby number, the Ekman boundary layers would start to be disrupted. Previous work has examined the Ekman boundary layer in straight channels (e.g., Johnson and Sandford, 1992; Wåhlin, 2004; Cossu et al., 2010, 2013). However, the detailed influence of bend curvature and centrifugal forces on Ekman boundary layers has yet to be addressed. The bulk secondary flow will lead to the migration of the downstream high velocity core to the

right hand side (upslope) as looking downstream (in the northern hemisphere). Such helical flow cells, in parallel with sedimentation on the downslope side (as suggested by the occurrence of overbank deposits along this region), act to focus erosion on the upslope side. There are a series of erosional terminations (blue dots in Figs. 5A and 6A) showing that the position and strength of this high-velocity core changes with time, reflecting changes in the velocity and excess density of the contour current over time.

## 8. Conclusions

This study documents, from a joint 3D seismic and oceanographic perspective, flow processes and in turn sedimentation in contourite channels on the northwestern South China Sea margin. Our results suggest that NPDW-CCs flowing through bends of contourite channels around a topographic high would yield an imbalance, through the flow depth, of upslope directed Coriolis forces versus downslope directed pressure-gradient and centrifugal forces. This, in turn, drives a Coriolis force-induced helical flow rotation composed of a large-scale secondary cell (i.e., an upper return flow towards the downslope and a basal flow towards the upslope) and an Ekman boundary layers at the very base. This Coriolis force-induced helical flow circulation most likely favored downslope deposition and resultant aerially extensive coverbank deposits along the downslope margins, but promoted upslope erosion and resultant asymmetric channel cross-sections with steepened channel walls and truncation terminations along upslope margins. Such asymmetric deposition-and-erosion patterns forced the studied channels to progressively migrate in an upslope direction, resulting

---

in clear upslope migration. Furthermore, the Coriolis force-induced helical flow rotation exhibits subcritical flow conditions (estimated as  $F_r$  of 0.04 to 0.17), and is sufficiently overbank to spill out of the studied contourite channels, yielding overbank deposits along the downslope flanks of the contourite channels.

ACCEPTED MANUSCRIPT

**Acknowledgments**

C. Gong appreciates the State of Texas Advanced Resource Recovery (STARR) Project for its generous support of CG's research at UT Austin. We are indebted to journal Editor (Michele Rebesco) and four reviewers (Thierry Mulder, David J.W. Piper, and two anonymous reviewers) for their critical but constructive comments that significantly improved the quality of this paper and to Michele Rebesco for editorial handling. This research was partly funded by the National Natural Science Foundation of China (No. 41372115). C. Gong dedicates this work to Zhaohong Cheng and Julia (Ruoyu) Gong, whose labour and arrival, respectively, greatly encourage his vigorous pursuit of deep-water sedimentology and stratigraphy.

## References

- Brackenridge, R.E., Hernández-Molina, F.J., Stow, D.A.V., Llave, E., 2013. A Pliocene mixed contourite-turbidite system offshore the Algarve Margin, Gulf of Cadiz: Seismic response, margin evolution and reservoir implications. *Marine and petroleum Geology* 46, 36–50.
- Clift, P., Gaedicke, C., 2002. Accelerated mass flux to the Arabian Sea during the middle to late Miocene. *Geology* 30, 207–210.
- Corney, R.T., Peakall, J., Parsons, D.R., Elliott, L., Amos, K.J., Best, J.L., Keevil, G.M., Ingham, D.B., 2006. The orientation of helical flow in curved channels. *Sedimentology* 53, 249–257.
- Corney, R.K.T., Peakall, J., Parsons, D.R., Elliott, L., Best, J.L., Thomas, R.E., Keevil, G.M., Ingham, D.B., Amos, K.J., 2008. Reply to discussion of Imran et al. on “The orientation of helical flow in curved channels” by Corney et al., *Sedimentology*, 53, 249–257. *Sedimentology* 55, 241–247.
- Cossu, R., Wells, M.G., 2010. Coriolis forces influence the secondary circulation of gravity currents flowing in large-scale sinuous submarine channel systems. *Geophysical Research Letters* 37, L17603.
- Cossu, R., Wells, M.G., 2013. The evolution of submarine channels under the influence of Coriolis forces: Experimental observations of flow structures. *Terra Nova* 25, 65–7.
- Cossu, R., Wells, M.G., Wåhlin, A.K., 2010. Influence of the Coriolis force on the velocity structure of gravity currents in straight submarine channel systems. *Journal of Geophysical Research* 115, C11016. <http://dx.doi.org/10.1029/2010JC006208>.
- Cossu, R., Wells, M.G., Peakall, J., 2015. Latitudinal variations in submarine channel sedimentation patterns: The role of Coriolis forces. *Journal of the Geological Society* 172, 161–174.
- Dorrell, R.M., Darby, S.E., Peakall, J., Sumner, E.J., Parsons, D.R., Wynn, R.B., 2013. Superelevation and overspill control secondary flow dynamics in submarine channels. *Journal of Geophysical Research: Oceans* 118, 3895–3915.
- Dykstra, M., Kneller, B., 2009. Lateral accretion in a deep-marine channel complex: implications for channelized flow processes in turbidity currents. *Sedimentology* 56, 1411–1432.
- Ezz, H., Cantelli, A., Imran, J., 2013. Experimental modeling of depositional turbidity currents in a sinuous submarine channel. *Sedimentary Geology* 290, 175–187.
- Ezz, H., Imran, J., 2014. Curvature-induced secondary flow in submarine channels. *Environmental Fluid Mechanics* 14, 343–370.
- Ezz, H., Cantelli, A., Imran, J., 2014. A polynomial model for lateral thickness decay of submarine channel-levees. *Journal of Sedimentary Research* 84, 51–57.
- Faugères, J.-C., Mezeraï, M.L., Stow, D.A.V., 1993. Contourite drift types and their distribution in the North and South Atlantic Ocean basins. *Sedimentary Geology* 82, 189–203.
- Faugères, J.-C., Stow, D.A.V., Imbert, P., Viana, A., 1999. Seismic features diagnostic of contourite drifts. *Marine Geology* 162, 1–38.
- Faugères, J.-C., Stow, D.A. V., 2008. Contourite drifts: Nature, evolution and controls. In: Rebesco, M., Camerlenghi, A. (Eds.), *Contourites. Developments in Sedimentology*, 60. Elsevier, Amsterdam, pp. 259–288.
- Galy, V., France-Lanord, C., Beyssac, O., Faure, P., Kufass, H., Palhol, F., 2007. Efficient organic burial in the Bengal Fan sustained by the Himalayan erosional system. *Nature* 450, 407–410.
- Giorgio Serchi, F., Peakall, J., Ingham, D.B., Burns, A.D., 2011. A unifying computational fluid dynamics investigation on the river-like to river-reversed secondary circulation in submarine channel bends. *Journal of Geophysical Research* 116, C06012.
- Gong, C., Wang Y., Zhu, W., Li, W., Xu, Q., 2013. Upper Miocene to Quaternary unidirectionally migrating deep-water channels in the Pearl River Mouth Basin, northern South China Sea. *AAPG Bulletin* 97, 285–308.

- Gong, C., Wang Y., Hodgson, D.M. Zhu, W., Li, W., Xu, Q., Li, D., 2014. Origin and anatomy of two different types of mass-transport complexes: A 3D seismic case study from the northern South China Sea margin. *Marine and Petroleum Geology* 54, 198–215
- Gong, C., Wang, Y., Xu, S., Pickering, K.T., Peng, X., Li, W., Yan, Q., 2015. The northeastern South China Sea margin created by the combined action of downslope and alongslope processes: Processes, products and implications for exploration and paleoceanography. *Marine and Petroleum Geology* 64, 233–249.
- Gong, C., Wang, Y., Steel, R., Peakall, J., Zhao, X., Sun, Q., 2016. Flow processes and sedimentation in unidirectionally migrating deep-water channels: From a three-dimensional seismic perspective. *Sedimentology* 63, 645–661.
- He, Y., Xie, X., Kneller, B.C., Wang, Z., Li, X., 2013. Architecture and controlling factors of canyon fills on the shelf margin in the Qiongdongnan Basin, northern South China Sea. *Marine and Petroleum Geology* 41, 264–276.
- Heezen, B.C., Hollister, C.D., 1964. Deep sea current evidence from abyssal sediments. *Marine Geology* 1, 141–174.
- Hernández-Molina, F.J., Stow, D.A.V., Alvarez-Zarikian, C.A., Acton, G., Bahr, A., Balestra, B., Ducassou, E., Flood, R., Flores, J.A., Furota, S., Grunert, P., Hodell, D., Jimenez-Espejo, F., Kim, J.K., Krissek, L., Kuroda, J., Li, B., Llave, E., Lofi, J., Lourens, L., Miller, M., Nanayama, F., Nishida, N., Richter, C., Roque, C., Pereira, H., Sanchez Goñi, M.F., Sierro, F.J., Singh, A.D., Sloss, C., Takashimizu, Y., Tzanova, A., Voelker, A., Williams, T., Xuan, C., 2014. Onset of Mediterranean Outflow into the North Atlantic. *Science* 344, 1244–1250.
- Imran, J., Islam, M.A., Huang, H., Kasseem, A., Dickerson, J., Pirmez, C., Parker, G., 2007. Helical flow couplets in submarine gravity underflows. *Geology* 35, 659–662.
- Janocko, M., Cartigny, M.B.J., Nemec, W., Hansen, E.W.M., 2013. Turbidity current hydraulics and sediment deposition in erodible sinuous channels: Laboratory experiments and numerical simulations. *Marine and Petroleum Geology* 41, 222–249.
- Johnson, G.C., Sanford, T.B., 1992. Secondary circulation in the Faroe bank channel outflow. *Journal of Physical Oceanography* 22, 927–933.
- Kane, I., Mayall, M., McCaffrey, B., 2013. Internal architecture, bedforms and geometry of turbidite channels. A conference held at the Geological Society, London, June 20–21<sup>st</sup> 2011. *Marine and Petroleum Geology* 41, 1–6.
- Keevil, G.M., Peakall, J., Best, J.L., Amos, K.J., 2006. Flow structure in sinuous submarine channels: Velocity and turbulence structure of an experimental submarine channel. *Marine Geology* 229, 241–257.
- Kneller, B., 2003. The influence of flow parameters on turbidite slope channel architecture. *Marine and Petroleum Geology* 20, 901–910.
- Kneller, B., Buckee, C., 2000. The structure and fluid mechanics of turbidity currents: A review of some recent studies and their geological implications. *Sedimentology* 47, 62–94.
- Li, H., Wang, Y., Zhu, W., Xu, Q., He, Y., Tang, W., Zhuo, H., Wang, D., Wu, J., Li, D., 2013. Seismic characteristics and processes of the Plio-Quaternary unidirectionally migrating channels and contourites in the northern slope of the South China Sea. *Marine Petroleum Geology* 43, 370–380.
- Liu, F., Wu, L., 2006. Xisha Trough in the southwestern South China Sea: Topographic and morphologic characteristics and genesis. *Marine and Quaternary Geology* 26, 7–13 (in Chinese with English abstract).
- McHargue, T., Pycrz, M.J., Sullivan, M.D., Clark, J.D., Fildani, A., Romans, B.W., Covault, J.A., Levy, M., Posamentier, H.W., Drinkwater, N.J., 2011. Architecture of turbidite channel systems on the continental slope: Patterns and predictions. *Marine and Petroleum Geology* 28, 728–743.

- McCave, I.N., 2008. Size sorting during transport and deposition of fine sediments: sortable silt and flow speed. In: Rebesco, M., Camerlenghi, A. (Eds.), *Contourites. Developments in Sedimentology*, 60. Elsevier, Amsterdam, pp. 379–407.
- Menard, H.W., 1955. Deep-sea channels, topography, and sedimentation. *AAPG Bulletin* 39, 236–255.
- Mohrig, D., Buttles, J., 2007. Deep turbidity currents in shallow channels. *Geology* 35, 155–158.
- Mulder, T., Voisset, M., Lecroart, P., Le Drezen, E., Gonthier, E., Hanquiez, V., Faugères, J.-C., Habgood, E., Hernández-Molina, F., Estrada, F., Llave-Barranco, E., Poirier, D., Gorini, C., Fuchey, Y., Voelker, A., Freitas, P., Sanchez, F., Fernandez, L., Kenyon, N., Morel, J., 2003. The Gulf of Cadiz: An unstable giant contouritic levee. *Geo-Marine Letters* 23, 7–18.
- Normark, W.R., 1970. Growth patterns of deep-sea fans. *AAPG Bulletin* 54, 2170–2195.
- Parsons, D.R., Peakall, J., Aksu, A.E., Flood, R.D., Hiscott, R.N., Besiktepe, S., Mouland, D., 2010. Gravity-driven flow in a submarine channel bend: Direct field evidence of helical flow reversal. *Geology* 38, 1063–1066.
- Peron-Pinvidic, G., Manatschal, G., Osmundsen, P.T., 2013. Structural comparison of archetypal Atlantic rifted margins: A review of observations and concepts. *Marine and Petroleum Geology* 43, 21–47.
- Peakall, J., McCaffrey, W.D., Kneller, B.C., 2000. A process model for the evolution, morphology, and architecture of sinuous submarine channels. *Journal of Sedimentary Research* 70, 434–448.
- Peakall, J., Amos, K.J., Keevil, G.M., Bradbury, W., Gupta, S., 2007. Flow processes and sedimentation in submarine channel bends. *Marine and Petroleum Geology* 24, 470–486.
- Peakall, J., Kane, I.A., Masson, D.G., Keevil, G., McCaffrey, W., Corney, R., 2012. Global (latitudinal) variation in submarine channel sinuosity. *Geology* 40, 11–14.
- Peakall, J., Sumner, E.J., 2015. Submarine channel flow processes and deposits: A process-product perspective. *Geomorphology* 244, 95–120.
- Piper, D.J.W., Normark, W.R., 1983. Turbidite depositional patterns and flow characteristics, navy submarine fan, California borderland. *Sedimentology* 30, 681–694.
- Piper, D.J.W., Normark, W.R., 2001. Sandy fans—from Amazon to Hueneme and beyond. *AAPG Bulletin* 85, 1407–1438.
- Pyles, D.R., Tomasso, M., Jennette, D.C., 2012. Flow processes and sedimentation associated with erosion and filling of sinuous submarine channels. *Geology* 40, 143–146.
- Rebesco, M., 2005. Contourites. In: Selley, R.C., Cocks, L.R.M., Plimer, I.R., (Eds.), *Encyclopedia of Geology*, Volume 4, Elsevier, Oxford, pp. 513–527.
- Rebesco, M., Hernández-Molina, F.J., Van Rooij, D., Wählin, A., 2014. Contourites and associated sediments controlled by deep-water circulation processes: State of the art and future considerations. *Marine Geology* 352, 111–154.
- Sumner, E., Peakall, J., Dorrell, R.M., Parsons, D.R., Wynn, R.B., Darby, S.E., McPhail, S.D., Perrett, J., Webb, A., White, D., 2014. Driven around the bend, spatial evolution and controls on the orientation of helical bend flow in a natural submarine gravity current. *Journal of Geophysical Research-Oceans* 119, 898–913.
- Sylvester, Z., Covault, J.A., 2016. Development of cutoff-related knickpoints during early evolution of submarine channels. *Geology* 44, 835–838, doi:10.1130/G38397.1.
- Shepard, F.P., Emery, K.O., 1973. Congo submarine canyon fan valley. *AAPG Bulletin* 57, 1679–1691.
- Shanmugam, G., 2008. Deep-water bottom currents and their deposits. In: Rebesco, M., Camerlenghi, A. (Eds.), *Contourites. Developments in Sedimentology*, 60. Elsevier, Amsterdam, pp. 59–83.
- Stow, D.A.V., Hunter, S., Wilkinson, D., Hernández-Molina, F.J., 2008. The nature of contourite deposition. In: Rebesco, M., Camerlenghi, A. (Eds.), *Contourites. Developments in Sedimentology*, 60. Elsevier, Amsterdam,

pp. 223–256.

- Stow, D.A.W., Hernández-Molina, F.J., Lave, E., Bruno, M., García, M., Díaz del Rio, V., Somoza, L., Brackenridge, R.E., 2013. The Cadiz Contourite Channel: Sandy contourites, bedforms and dynamic current interaction. *Marine Geology* 343, 99–114.
- Thomson, R., Davis, E., Heesemann, M., Villinger, H., 2010. Observations of long duration episodic bottom currents in the Middle America Trench: Evidence for tidally initiated turbidity flows. *Journal of Geophysical Research: Oceans* 115, C10020.
- Vangriesheim, A., Khripounoff, A., Crassous, P., 2009. Turbidity events observed in situ along the Congo submarine channel, *Deep Sea Research, Part II* 56, 2208–2222
- Viana, A.R., Faugères, J.-C., Stow, D.A.V., 1998. Bottom-current controlled sand deposits: a review from modern shallow to deep water environments. *Sedimentary Geology* 115, 53–80.
- Wynn, R.B., Cronin B.T., Peakall J., 2007. Sinuous deep-water channels: Genesis, geometry and architecture, *Marine and Petroleum Geology* 24, 341–387.
- Wählin, A.K., 2004. Downward channeling of dense water in topographic corrugations, *Deep Sea Research Part I* 51, 577–590.
- Yang, Q., Tian, J., Zhao, W., 2010. Observation of Luzon Strait transport in summer 2007. *Deep-Sea Research Part I* 57, 670–676
- Zhao, Z., Sun, Z., Wang, Z., Sun, Z., Liu, J., Zhang, C., 2015a. The high resolution sedimentary filling in Qiongdongnan Basin, Northern South China Sea. *Marine Geology* 361, 11–24.
- Zhao, Y., Liu, Z., Zhang, Y., Lia, J., Wang, M., Wang, W., Xu, J., 2015b. In situ observation of contour currents in the northern South China Sea: Applications for deepwater sediment transport. *Earth and Planetary Science Letters* 430, 477–485.
- Zhu, M., Graham, S., Pang, X., McHargue, T., 2010. Characteristics of migrating submarine canyons from the middle Miocene to present: Implications for paleoceanographic circulation, Northern South China Sea. *Marine and Petroleum Geology* 27, 307–319.

## Figure captions

**Fig. 1.** (A) Bathymetric map (provided by Guangzhou Marine Geological Survey) showing geographical context of the study area (solid box with red outline) along the northwestern South China Sea margin. Also shown are regional plan-view locations of bathymetric maps (Fig. 1B) and geomorphic images (Figs. 8 to 10). Pathways of the North Pacific Intermediate Water (NPIW) and North Pacific Deep Water (NPDW) are from Gong et al. (2013, 2015). (B) Bathymetric map of the modern seafloor of the study area showing map-view locations of seismic sections presented in Figs. 5A, 5B, 6A, 6B, 11A, 11B, and 14A. Also shown are plan-view locations of bathymetric maps shown in Figs. 2 and 15A and time slices presented in Figs. 3 and 4. Note that time slices shown in Figs. 8 to 10, together with bathymetric map of Fig. 1B, cover the full 3D seismic survey marked by the solid box in Fig. 1A, but that time slices shown in Figs. 3 and 4 (marked by red boxes in Fig. 1B) only cover a part of the 3D seismic survey.

**Fig. 2.** Three-dimensional perspective of time structure diagram of the modern seafloor (map location shown in Fig. 1B) illustrating plan-view morphology of contourite channels (alongslope seismic facies) and overbank deposits (overbank seismic facies). Hot and cool colours for the depth scale correspond to topographic highs and lows, respectively (also in the bathymetric maps of Figs. 1B and 15A).

**Fig. 3.** Flattened horizontal amplitude slices (plan-view locations shown in Figs. 1B and 8A to 10A) taken at 24 ms (A) and 132 ms (B) below the modern seafloor illustrating plan-view geomorphological characteristics of contourite channels and concomitant overbank deposits. Note that the seismic horizon slice of Fig. 3A may not strictly follow the seismic reflection of the modern seafloor, giving rise to closely spaced, wavy seismic reflection patterns.

**Fig. 4.** Flattened horizontal amplitude slices (plan-view locations shown in Figs. 1B and 8A to 10A) seen at 168 ms (A) and 250 ms (B) below the modern seafloor

showing plan-view geomorphological characteristics of contourite channels and concomitant overbank deposits.

**Fig. 5.** Dip- and strike-view seismic lines (panels A and B, respectively) illustrating cross-sectional seismic manifestations of contourite channels (alongslope seismic facies) and contemporaneous overbank deposits (overbank seismic facies). The small blue dots represent the base of the overbank facies. See Figs. 1B, 3 to 4, and 8A to 10A for line locations.

**Fig. 6.** Dip- and strike-orientated seismic sections (panels A and B, respectively) showing cross-sectional seismic expression of contourite channels (alongslope seismic facies) and contemporaneous overbank deposits (overbank seismic facies). The small blue dots represent the base of the overbank facies. See line locations in Figs. 1B, 3 to 4, and 8A to 10A. (C) The enlarged seismic section illustrating a close-up view of levee crests with downlap terminations (red dots) and overlying levee crest draping imaged as well-layered, parallel to subparallel, continuous reflections.

**Fig. 7.** (A) Plots of average width ( $W$ ) versus average thickness ( $T$ ) for contourite channels (red triangles) and unidirectionally migrating deep-water channels (blue dots). (B) Plots of channel aspect ratios ( $W/T$ ) against average thickness ( $T$ ) for contourite channels (red triangles) and unidirectionally migrating deep-water channels (blue dots). Refer to Tables 2 and 3 for full details. A t-test, conducted at a confidence interval of 95%, concludes the populations to be statistically distinctive either by  $W$ ,  $T$  or by  $W/T$ .

**Fig. 8.** Flattened horizontal seismic amplitude (panel A) and RMS-attribute slices (panel B) seen at 150 ms (TWTT) below the modern seafloor (for location see Fig. 1A) showing plan-view geomorphological manifestations of contourite channels, overbank deposits, and channel-complex set 1 (CCS1) of unidirectionally migrating deep-water channels.

**Fig. 9.** Flattened horizontal seismic amplitude (panel A) and RMS-attribute slices (panel B) taken at 170 ms (TWTT) below the modern seafloor (see Fig. 1A for location) illustrating plan-view geomorphological appearance of contourite channels, overbank deposits, and channel-complex set 1 (CCS1) of unidirectionally migrating deep-water channels.

**Fig. 10.** Flattened horizontal seismic amplitude (panel A) and RMS-attribute slices (panel B) seen at 180 ms (TWTT) below the modern seafloor (for location see Fig. 1A) showing plan-view geomorphological expression of contourite channels, overbank deposits, and channel-complex set 1 (CCS1) of unidirectionally migrating deep-water channels.

**Fig. 11.** Depositional strike- and dip-orientated seismic sections (upper and lower panels, respectively) showing cross-sectional seismic expression of unidirectionally migrating deep-water channels (i.e., downslope seismic facies). See Fig. 1B for line locations. In depositional strike view (A), unidirectionally migrating deep-water channels comprise two different channel-complex sets (CCS1 and CCS2); these consistently migrated from CCS2 to CCS1, and exhibit unidirectional channel trajectories. In depositional dip view (B), they are not linked to the coeval shelf edges, with their heads merging into the regional slope of the studied margin.

**Fig. 12.** Isopach maps (depicted by 10 m contours) of channel-complex sets (CCS1 and CCS2) of unidirectionally migrating deep-water channels (left and right panels, respectively).

**Fig. 13.** (A) Plots of  $V_a$  versus  $L_m$  for contourite- and unidirectionally migrating deep-water channels (red triangles and blue dots, respectively). (B)  $L_m/V_a$  against  $L_m$  for contourite channels and unidirectionally migrating deep-water channels (red triangles and blue dots, respectively).  $L_m$  and  $V_a$  refer to lateral and vertical components of a specific channel-growth trajectory, respectively. A t-test confirms that the differences between  $L_m$  and  $L_m/V_a$  populations are statistically significant with

a 95% confidence interval.

**Fig. 14.** (A) Two-dimensional seismic transects from 3D seismic volume (for line location see Figs. 1B, 3 to 4, and 8A to 10A) illustrating the cross-sectional seismic appearance of contourite channels and their associated overbank deposits. (B) Cartoon-style illustration of the cross-sectional view of the Coriolis force-induced helical flow rotation in the interpreted contourite channels. (C) Line drawing illustrating the main forces operating within contourite channels; shown for the northern hemisphere. The dominant Coriolis force, opposed by the pressure gradient and centrifugal force (blue arrows), leads to super-elevation on the right hand side of the channel, as looking downstream. The main helical cell, shown by the solid black line, is the result of these three opposing forces, with lower levels of the flow moving in the upslope (transverse) direction, and the upper flow moving downslope. At the basal and upper flow interfaces, Ekman boundary layers form (black straight arrows), and these are orientated in a downslope (transverse) direction. The basal Ekman boundary layer is particularly important for basal sediment transport. See text for further details. Figure based on Cossu et al., (2010) and Cossu and Wells (2010).

**Fig. 15.** (A) Three-dimensional perspective of time bathymetric map of the modern seafloor illustrating plain-view morphology of contourite channels around a topographic high and flow processes flowing through them. (B) Cartoon-style illustrations of the plan view of the Coriolis force-induced helical flow circulation in the studied contourite channels.

---

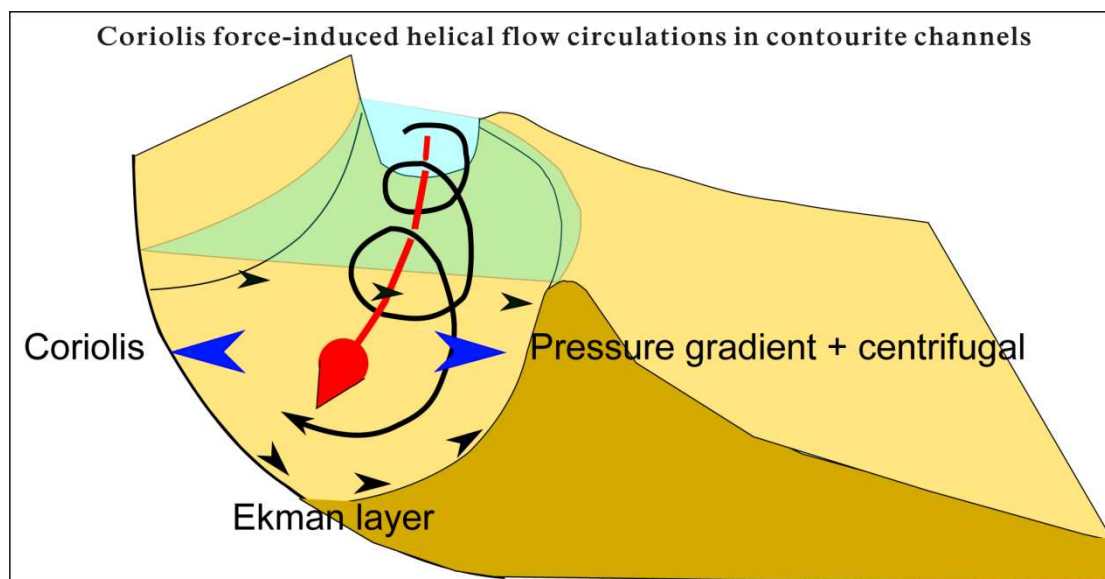
**Table captions**

**Table 1** Tabulation of seismic facies descriptions and interpretations.

**Table 2** Morphometric properties of contourite channels recognized as alongslope seismic facies.

**Table 3** Morphometric properties of two channel-complexes sets (CCS1 and CCS2) recognized in the unidirectionally migrating deep-water channels.

ACCEPTED MANUSCRIPT



Graphical abstract

ACCEPTED MANUSCRIPT

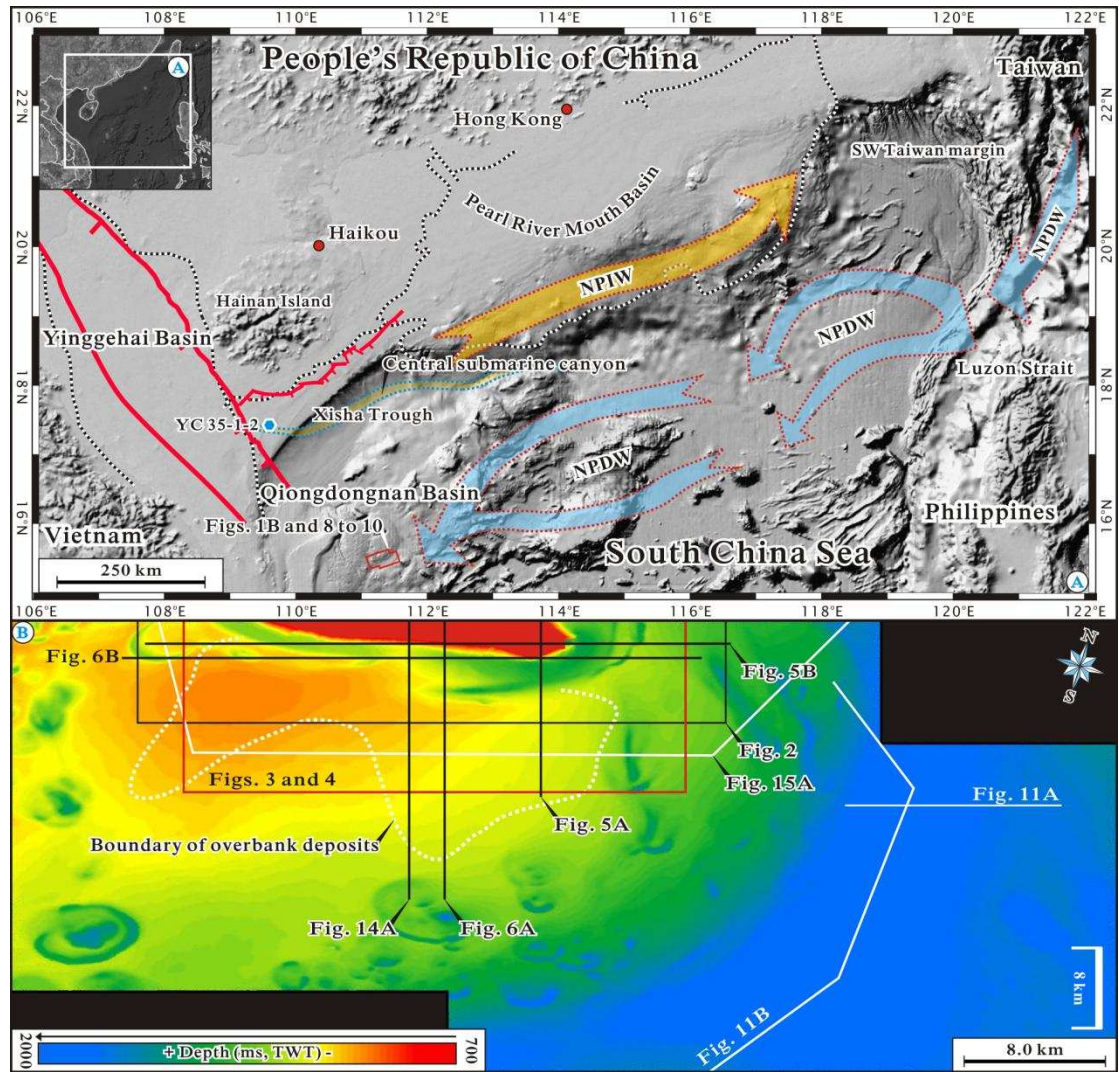


**Figure 1** (two-column width, color).

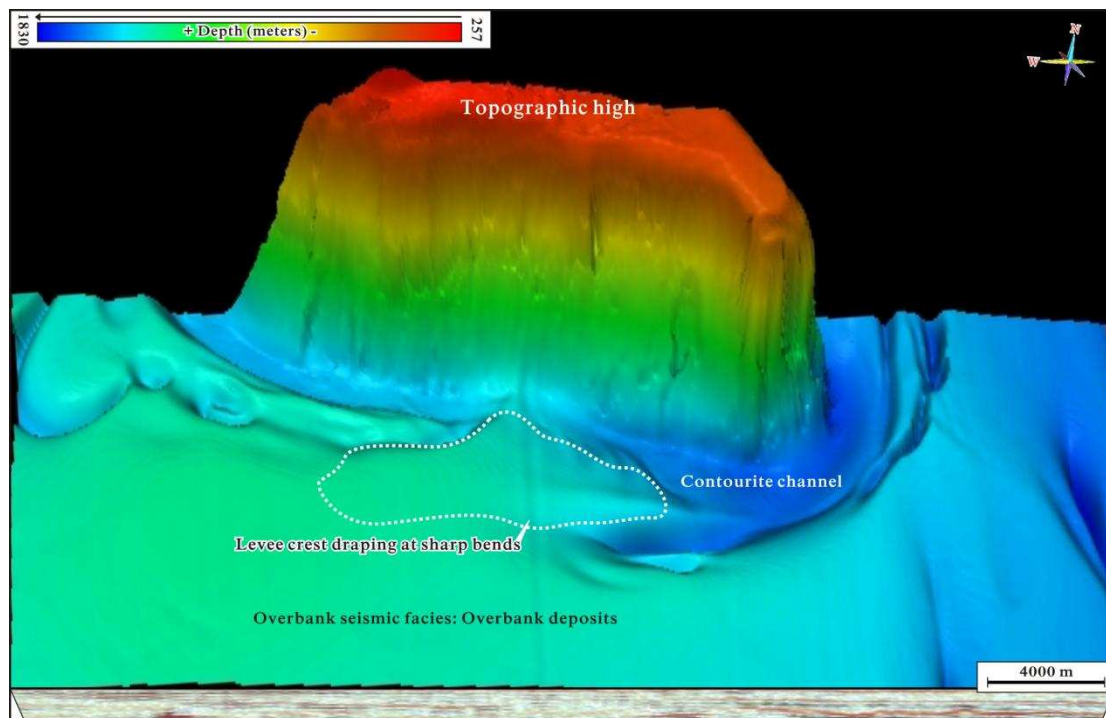


Figure 2 (two-column width, color).

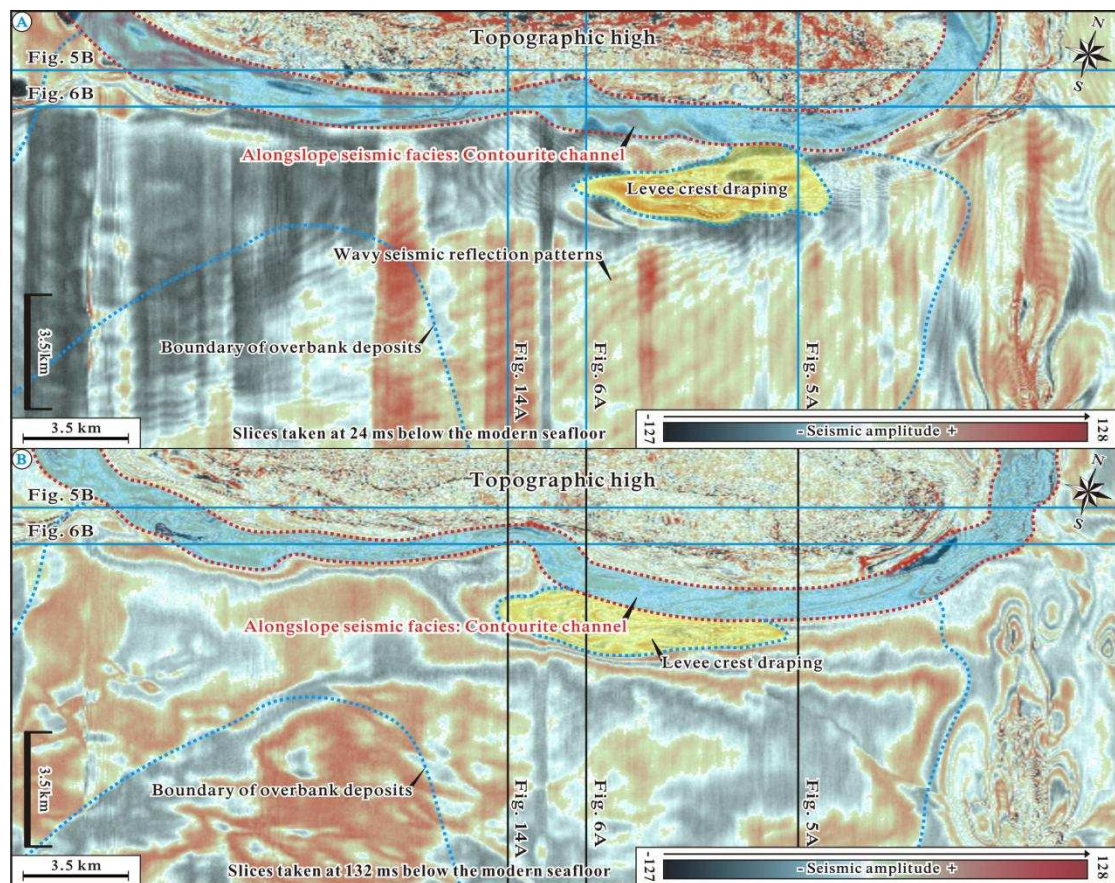


Figure 3 (two-column width, color).

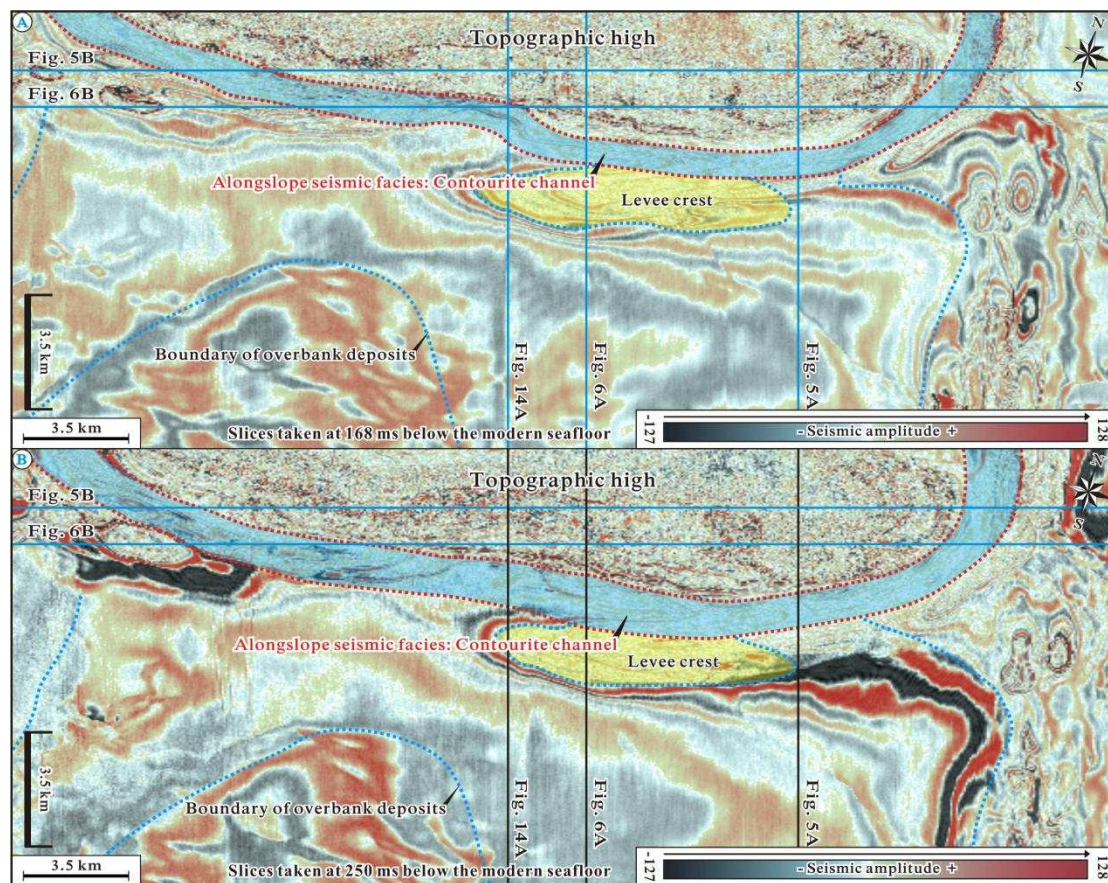


Figure 4 (two-column width, color).

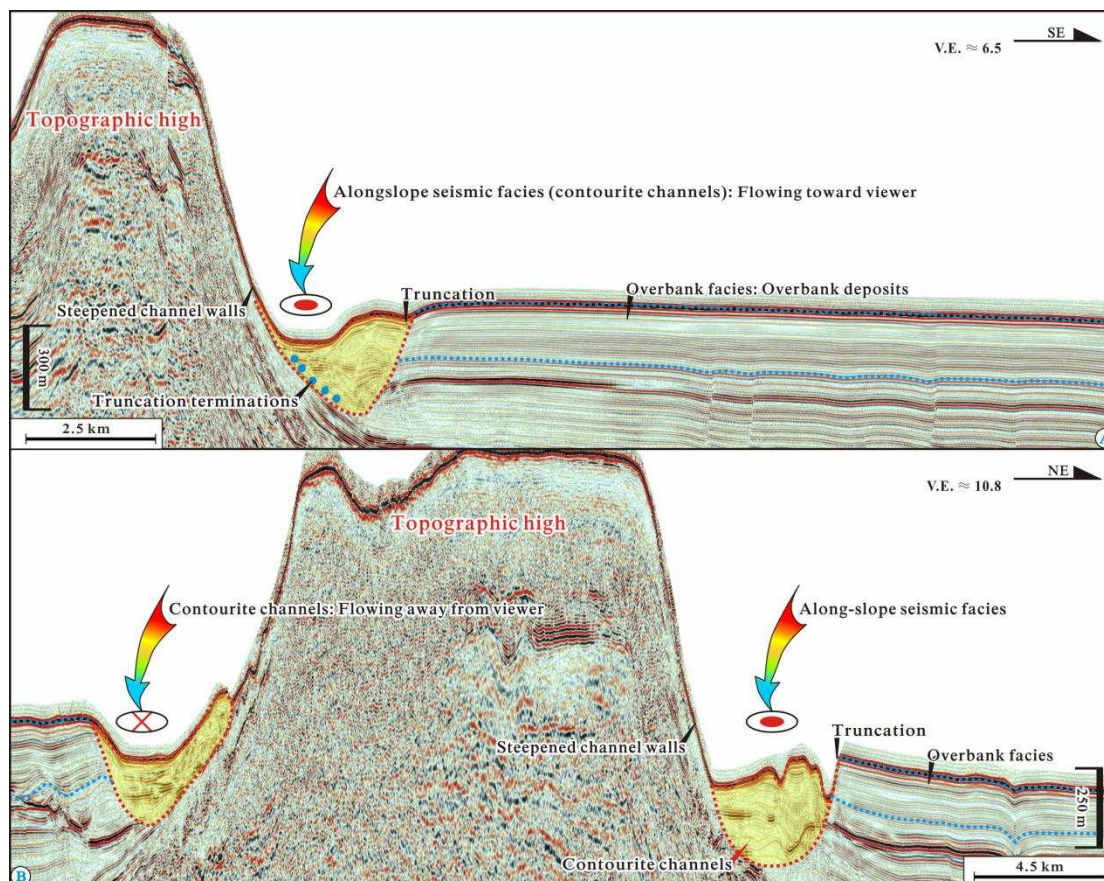


Figure 5 (two-column width, color).

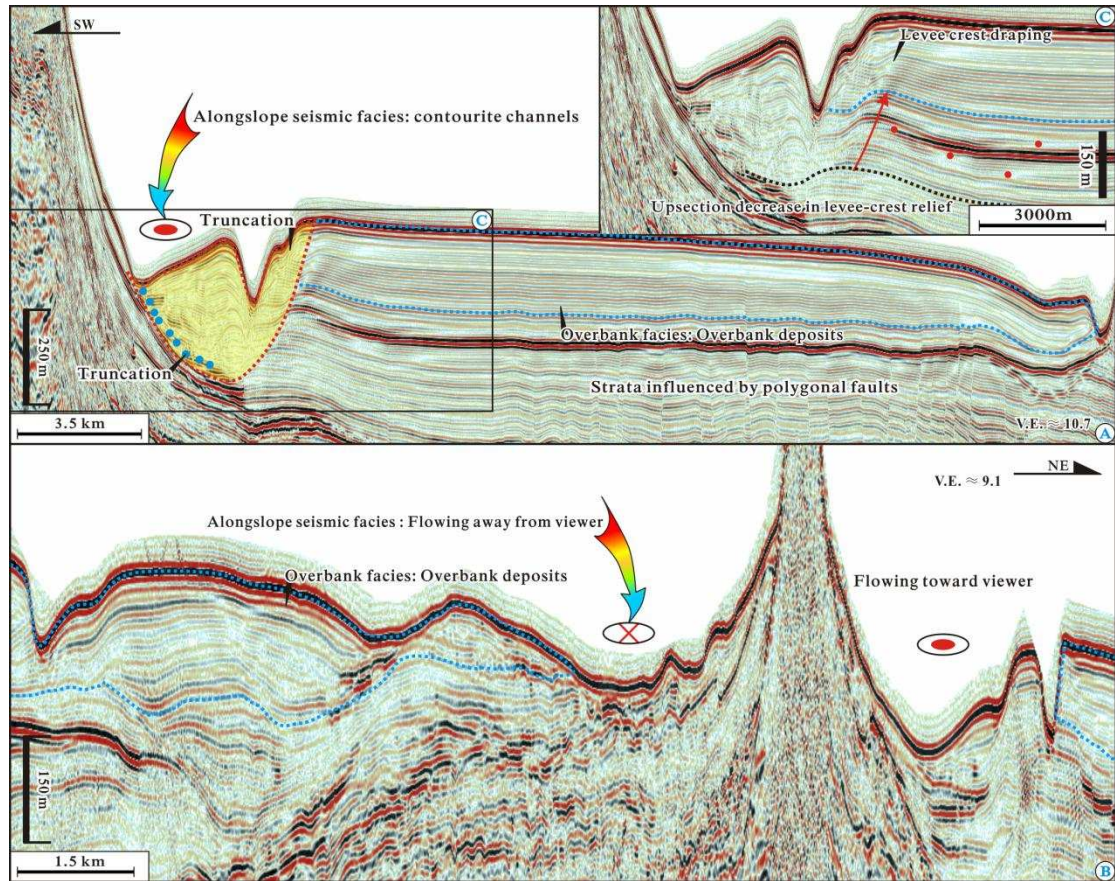
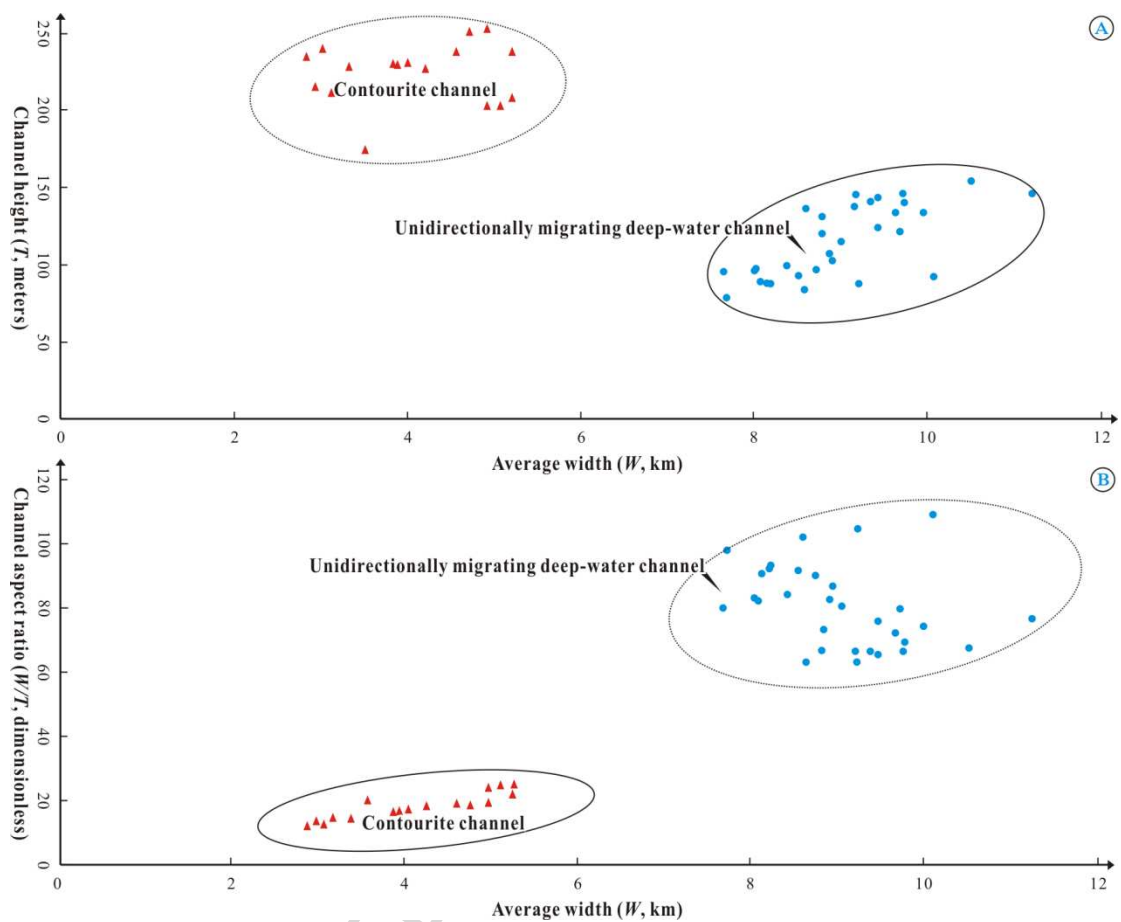


Figure 6 (two-column width, color).



**Figure 7** (two-column width, color).

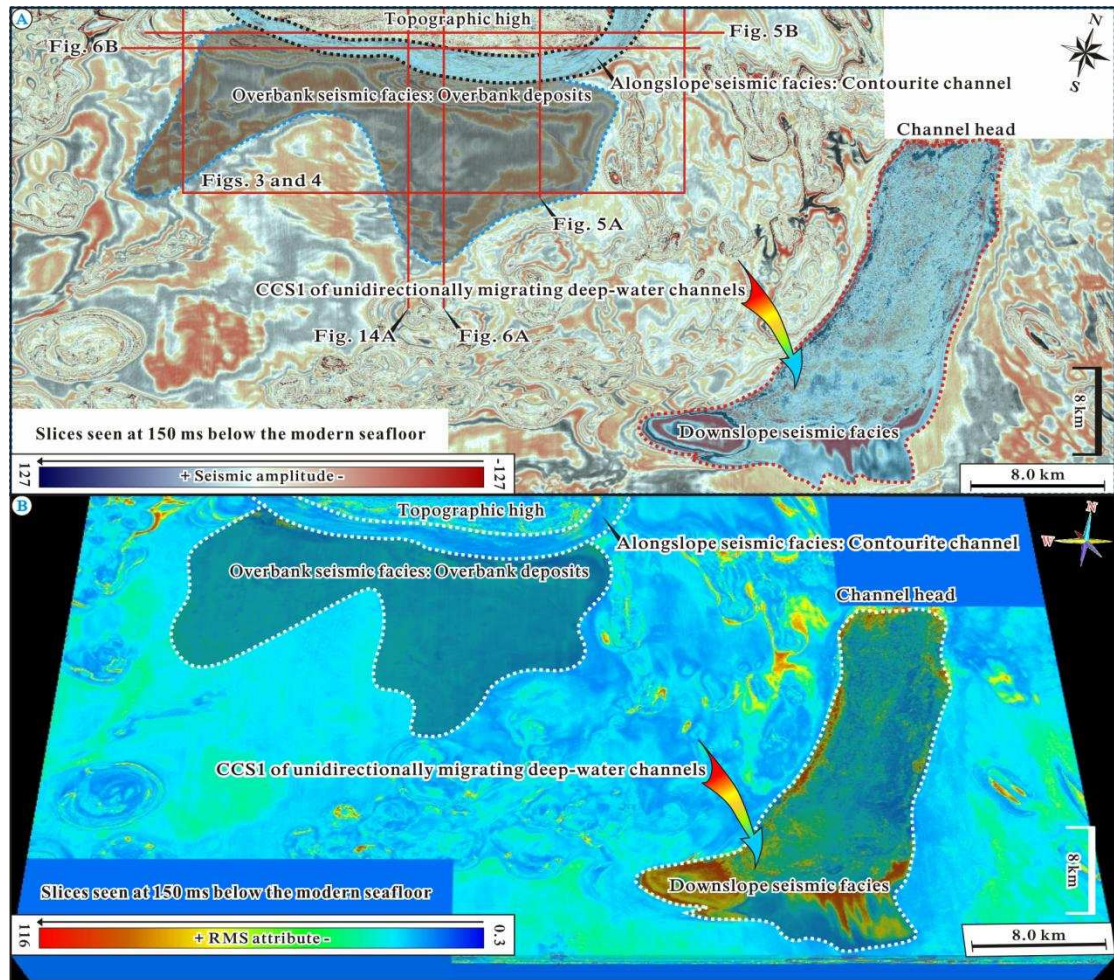


Figure 8 (two-column width, color).

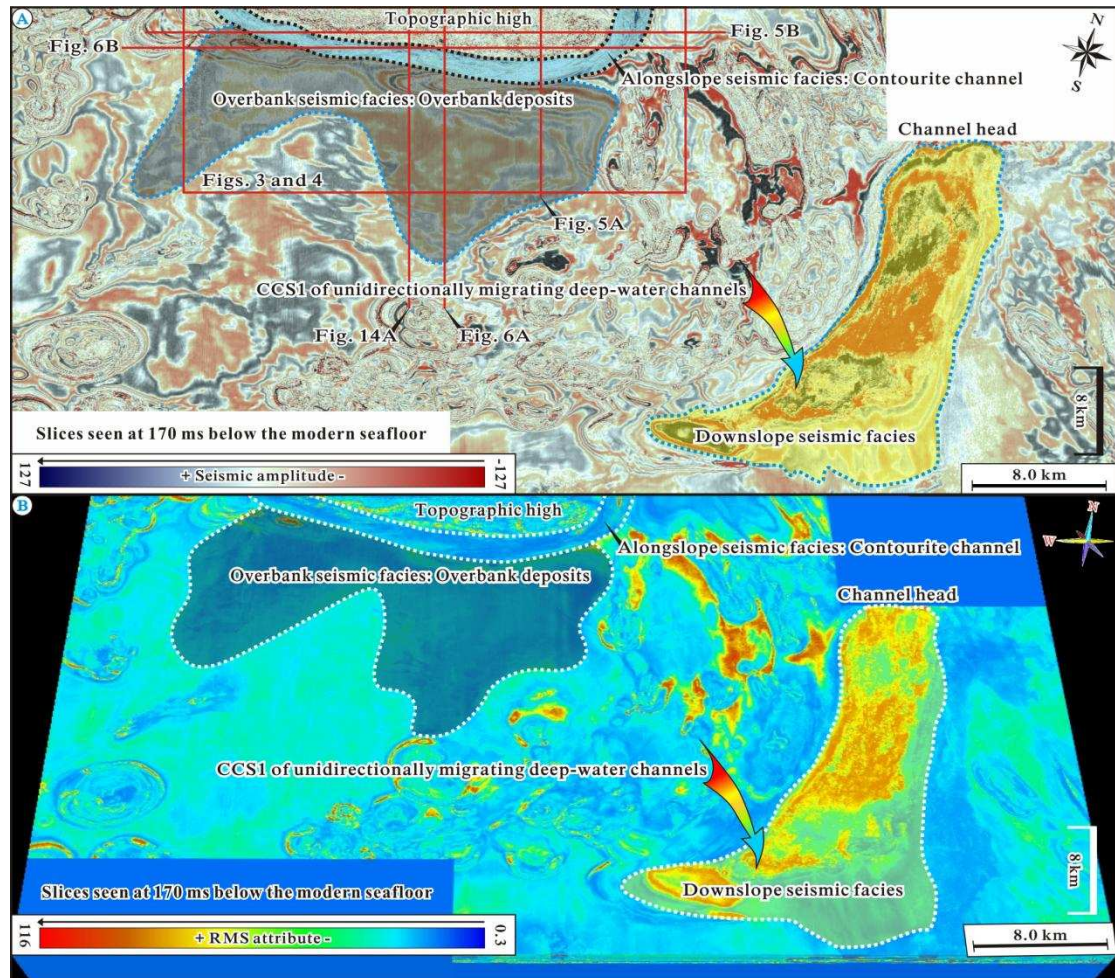


Figure 9 (two-column width, color).

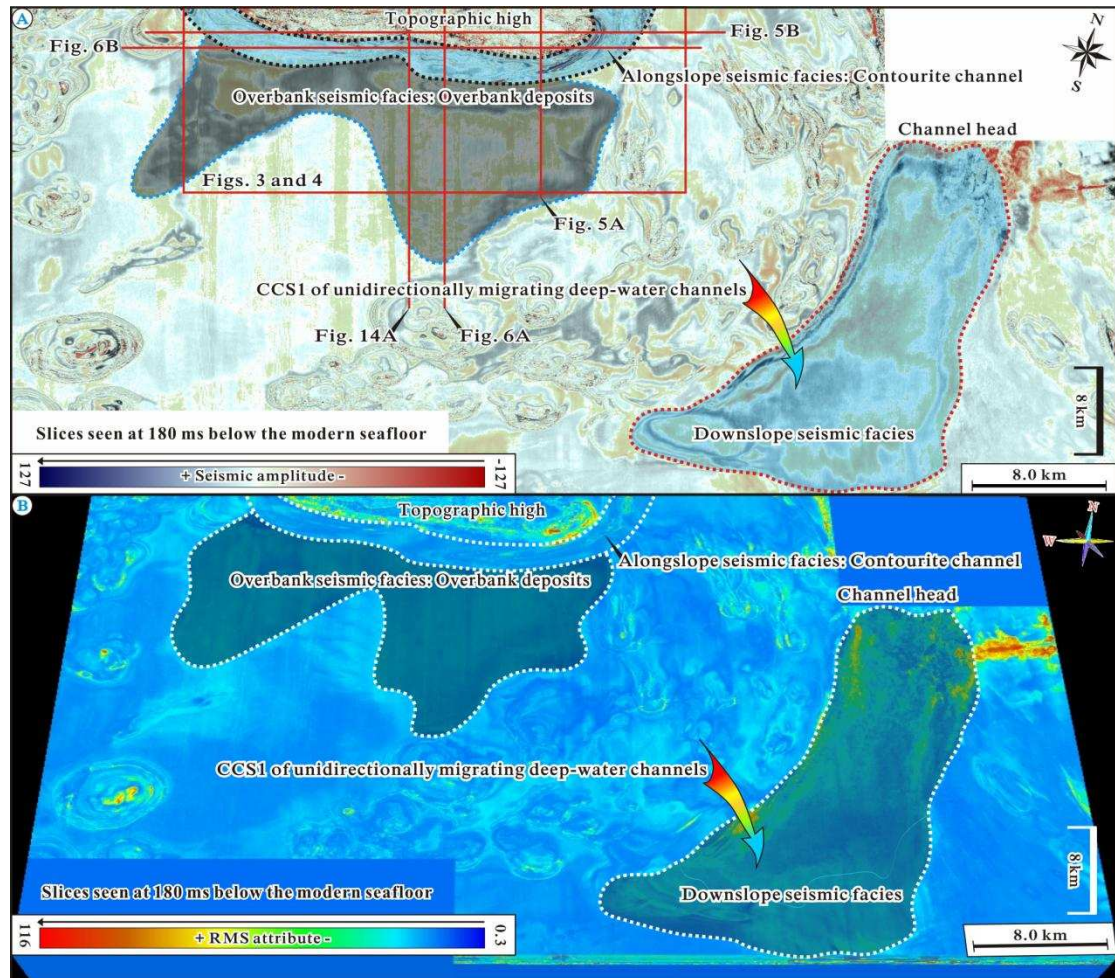


Figure 10 (two-column width, color).

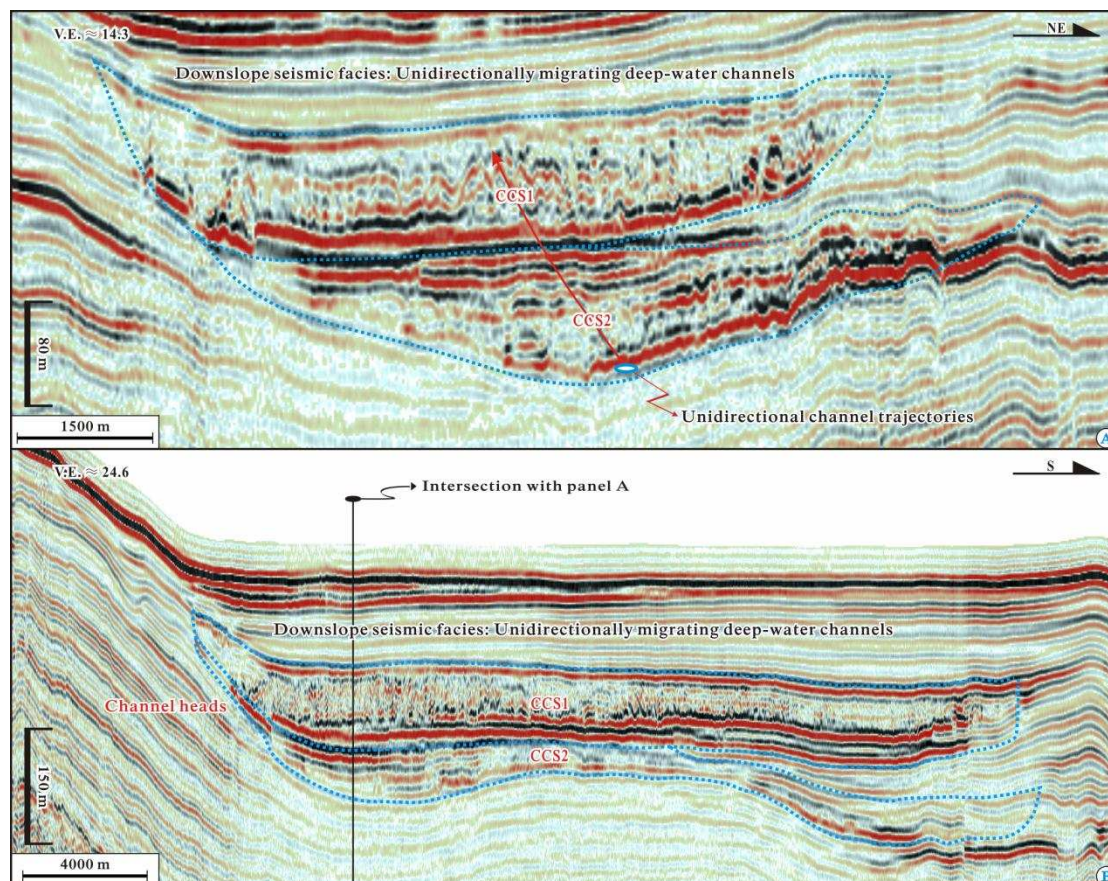


Figure 11 (two-column width, color).

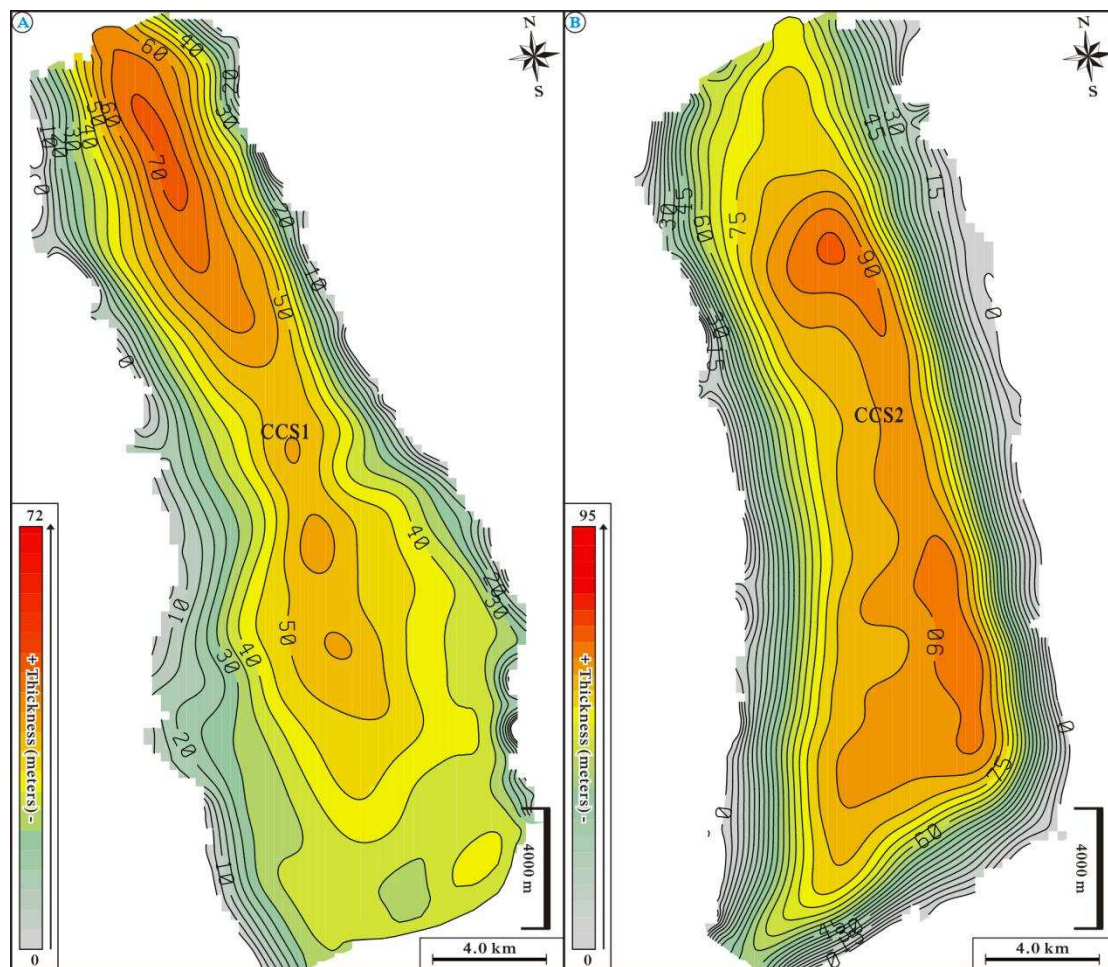
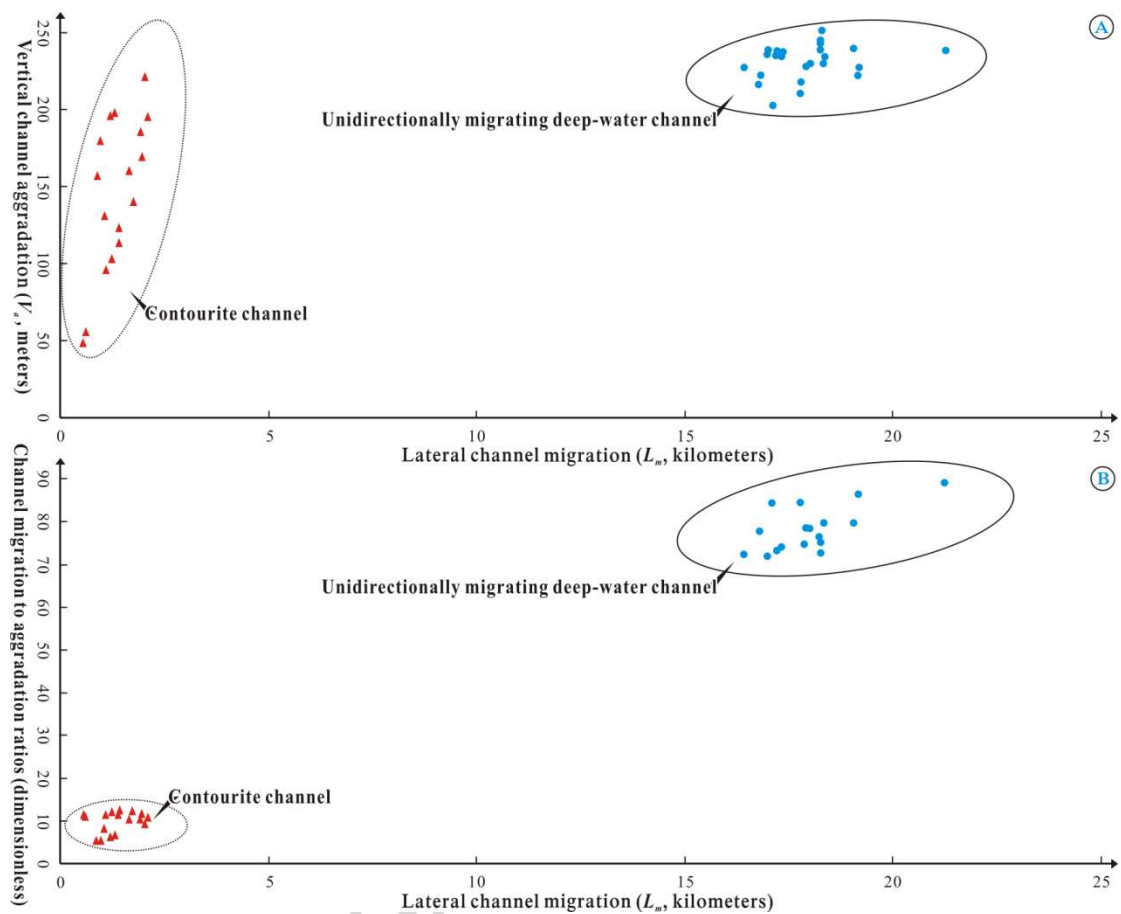


Figure 12 (two-column width, color).



**Figure 13** (two-column width, color).

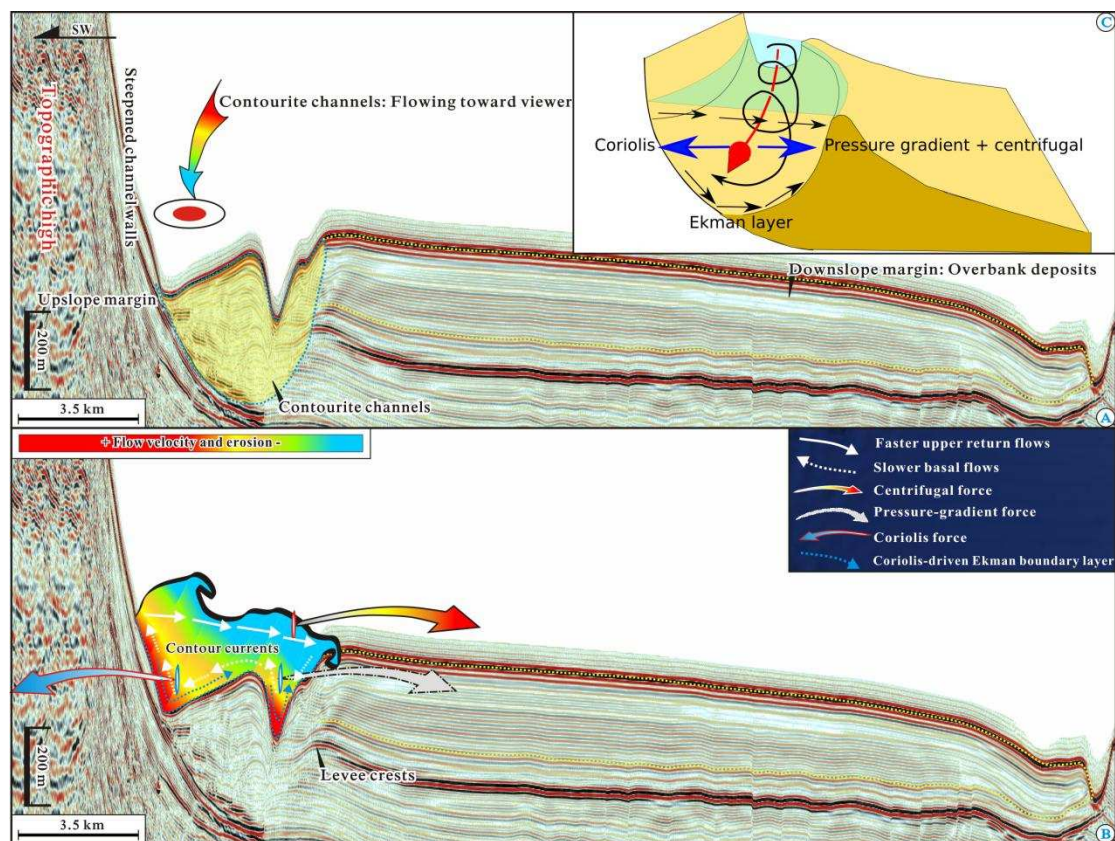


Figure 14 (two-column width, color).

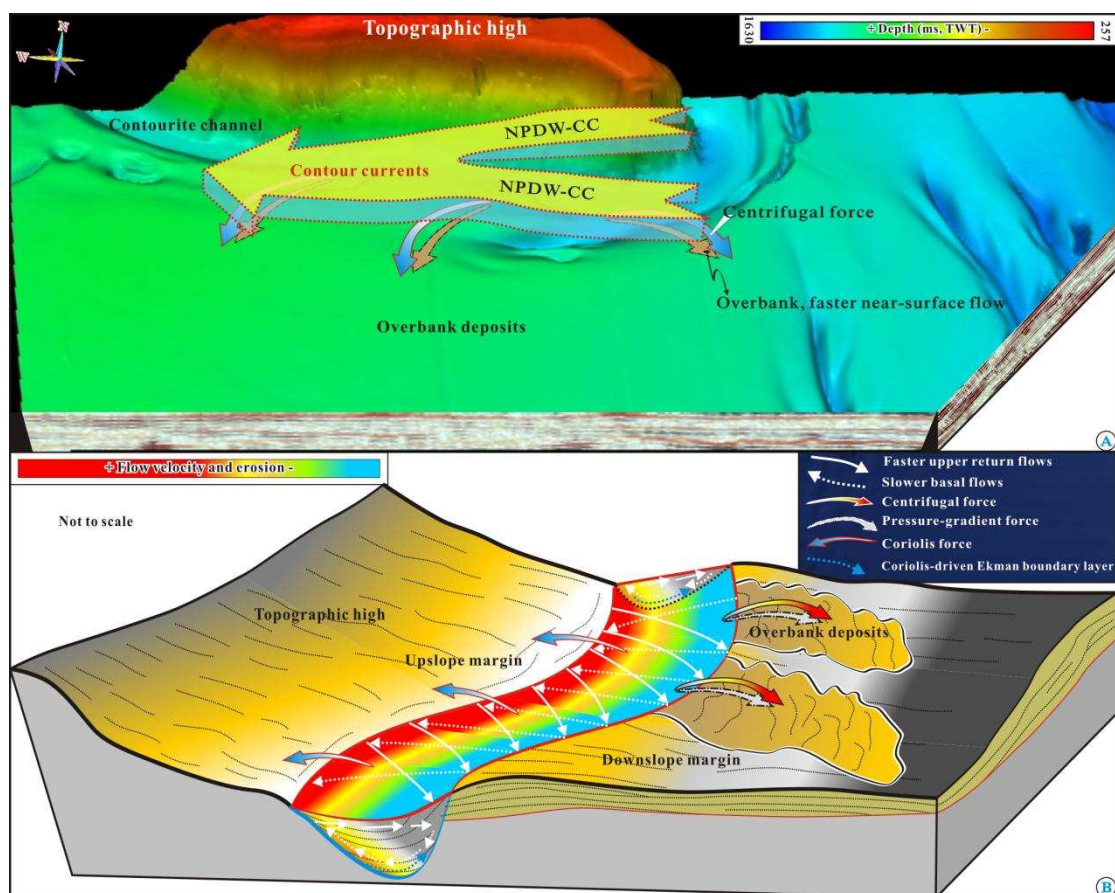


Figure 15 (two-column width, color).

**Table 1** (landscape).

Seismic facies	Cross-sectional seismic expression			Plan-view appearance		Seismic examples	Hydrodynamic interpretation
	Amplitude	Continuity	Geometry	RMS attribute maps	seismic amplitude maps		
Alongslope seismic facies	Low to moderate	Continuous	Lens-shaped, concave-up	Isobath-parallel, low RMS-attribute bands	Isobath-parallel, low amplitude bands	Figs. 3 to 6 and 8 to 10	Contour currents
Overbank seismic facies	Low	Continuous	Elongated, mounded	Low RMS-attribute tongues	Low amplitude tongues	Figs. 3 to 6 and 8 to 10	Contour currents
Downslope seismic facies	Large-scale incisions oriented roughly perpendicular to regional contour lines					Figs. 8 to 10 and 11	Interplay of contour and turbidity currents

**Table 2** (two-column width).

Seismic lines	Width (W, km)	Height (T, m)	W/T	Lateral migration ( $L_m$ , km)	Vertical aggradation ( $V_a$ , m)	$L_m/V_a$ (dimensionless)
Line 1720	3.0	240	13	1.0	180	5
Line 1760	2.8	235	12	0.9	157	6
Line 2040	4.6	239	19	1.9	185	10
Line 2080	5.2	238	22	2.0	221	9
Line 2250	3.8	231	17	1.3	198	7
Line 2280	4.0	231	17	1.2	196	6
Trace 5240	3.5	175	20	0.6	49	12
Trace 5260	4.9	203	24	1.1	96	11
Trace 5360	3.1	212	15	0.6	56	11
Trace 5440	4.7	251	19	1.2	103	12
Trace 5480	4.2	227	18	1.7	140	12
Trace 5500	3.9	230	17	1.4	113	13
Average	4.9	253	19	2.0	169	12
	3.3	229	15	1.4	124	11
	5.1	203	25	1.7	160	10
	2.9	216	14	1.1	131	8
	5.2	208	25	2.1	196	11
	4.1	225	18	1.4	146	10

**Table 3** (two-column width).

Seismic lines	CCSs	Width (W, km)	Height (T, m)	W/T	Lateral migration ( $L_m$ , km)	Vertical aggradation ( $V_a$ , m)	$L_m/V_a$ (dimensionless)
Line 3000	CCS1	10.1	92	109	21.3	238	89
	CCS2	11.2	146	77			
Line 3100	CCS1	9.2	88	105	19.2	222	86
	CCS2	10.0	134	74			
Line 3200	CCS1	8.6	84	102	19.1	240	80
	CCS2	10.5	155	67			
Line 3300	CCS1	8.1	89	91	17.8	210	84
	CCS2	9.7	121	80			
Line 3500	CCS1	8.2	88	93	17.9	228	79
	CCS2	9.7	140	69			
Line 3600	CCS1	7.7	79	98	17.1	203	84
	CCS2	9.4	124	76			
Line 3700	CCS1	8.0	96	83	16.8	216	78
	CCS2	8.8	120	73			
Line 3800	CCS1	8.9	103	87	18.2	243	75
	CCS2	9.3	141	66			
Line 3900	CCS1	8.9	107	83	18.3	251	73
	CCS2	9.4	144	66			
Line 4000	CCS1	8.5	93	92	18.2	239	76
	CCS2	9.7	146	67			
Line 4100	CCS1	8.7	97	90	18.3	230	80
	CCS2	9.6	134	72			
Line 4200	CCS1	8.4	99	84	17.0	236	72
	CCS2	8.6	136	63			
Line 4300	CCS1	8.2	89	92	17.3	234	74
	CCS2	9.2	146	63			
Line 4400	CCS1	8.0	97	82	17.2	235	73
	CCS2	9.2	138	66			
Line 4500	CCS1	7.7	96	80	16.4	227	72
	CCS2	8.8	131	67			
Average	CCSs	9.0	115	81	18.0	230	78

---

### Highlights

- Coriolis force-induced helical flow cell consists of a large-scale secondary cell and Ekman boundary layers at the very base.
- Coriolis force-induced helical flow cell exhibits unconfined, subcritical flow conditions.
- Coriolis force-induced helical flow cell yields downslope deposition versus upslope erosion.

ACCEPTED MANUSCRIPT